CrossMark

ORIGINAL ARTICLE

Multi-GNSS phase delay estimation and PPP ambiguity resolution: GPS, BDS, GLONASS, Galileo

Xingxing Li[1,2] · Xin Li[1] · Yongqiang Yuan[1] · Keke Zhang[1] · Xiaohong Zhang[1] · Jens Wickert[2]

Abstract This paper focuses on the precise point positioning (PPP) ambiguity resolution (AR) using the observations acquired from four systems: GPS, BDS, GLONASS, and Galileo (GCRE). A GCRE four-system uncalibrated phase delay (UPD) estimation model and multi-GNSS undifferenced PPP AR method were developed in order to utilize the observations from all systems. For UPD estimation, the GCRE-combined PPP solutions of the globally distributed MGEX and IGS stations are performed to obtain four-system float ambiguities and then UPDs of GCRE satellites can be precisely estimated from these ambiguities. The quality of UPD products in terms of temporal stability and residual distributions is investigated for GPS, BDS, GLONASS, and Galileo satellites, respectively. The BDS satellite-induced code biases were corrected for GEO, IGSO, and MEO satellites before the UPD estimation. The UPD results of global and regional networks were also evaluated for Galileo and BDS, respectively. As a result of the frequency-division multiple-access strategy of GLONASS, the UPD estimation was performed using a network of homogeneous receivers including three commonly used GNSS receivers (TRIMBLE NETR9, JAVAD TRE_G3TH DELTA, and LEICA). Data recorded from 140 MGEX and IGS stations for a 30-day period in January in 2017 were used to validate the proposed GCRE UPD estimation and multi-GNSS dual-frequency PPP AR. Our results show that GCRE four-system PPP AR

enables the fastest time to first fix (TTFF) solutions and the highest accuracy for all three coordinate components compared to the single and dual system. An average TTFF of 9.21 min with 7° cutoff elevation angle can be achieved for GCRE PPP AR, which is much shorter than that of GPS (18.07 min), GR (12.10 min), GE (15.36 min) and GC (13.21 min). With observations length of 10 min, the positioning accuracy of the GCRE fixed solution is 1.84, 1.11, and 1.53 cm, while the GPS-only result is 2.25, 1.29, and 9.73 cm for the east, north, and vertical components, respectively. When the cutoff elevation angle is increased to 30°, the GPS-only PPP AR results are very unreliable, while 13.44 min of TTFF is still achievable for GCRE four-system solutions.

1 Introduction

Precise point positioning (PPP) has been widely used for scientific research and civilian applications, such as GNSS meteorology, GNSS seismology, and precision agriculture (Zumberge et al. 1997; Kouba and Héroux 2001; Bisnath and Gao 2008; Li et al. 2014). However, the traditional float PPP needs an initialization time of more than 30 min to achieve centimeter-level positioning accuracy. In order to improve the positioning accuracy and shorten the initialization time, GPS PPP ambiguity resolution (AR) technique has been developed in recent years (Ge et al. 2008; Collins et al. 2008; Geng et al. 2009; Laurichesse et al. 2009; Li et al. 2011; Loyer et al. 2012; Li and Zhang 2012). The results show that compared with float solution, the dual-frequency GPS PPP AR solution based on undifferenced and uncombined observations

✉ Xingxing Li
  lxlq109121@gmail.com

1   School of Geodesy and Geomatics, Wuhan University, 129
    Luoyu Road, Wuhan 430079, Hubei, China

2   German Research Centre for Geosciences (GFZ),
    Telegrafenberg, 14473 Potsdam, Germany

Table 1 Overview of precision orbit and clock products of all MEGX analysis centers as of June 2017

Institution	Abbreviation	Satellites	Orbit (min)	Clock (min)
CNES/CLS	GRM	GRE	15	0.5
CODE	COM	GCREJ	15	5
GFZ	GFM	GE	15	5
	GBM	GCREJ	15/5	5/0.5
TUM	TUM	EJ	5	5
WU	WUM	GCREJ	15	5
ESA/ESOC	ESM	GCREJ	15	5
JAXA	QZF	GJ	5	5

The satellite system "G", "R", "E", "C", and "J" refer to the GPS, GLONASS, Galileo, BDS, and QZSS, respectively

can improve the 3D positioning accuracy by 54% from 4.8 to 2.2 cm, and shorten the convergence time by 32% from 31.6 to 21.4 min (Li et al. 2013).

Currently, the satellite navigation world is facing dramatic changes with the rapid development of multi-constellation Global Navigation Satellite Systems (GNSS). As of June 2017, 83 satellites are available. More than 120 navigation satellites will be in view with the four systems (GPS, BDS, GLONASS, and Galileo) fully deployed in coming years (Li et al. 2015). BeiDou Satellite Navigation System (BDS) is an independently developed and independently operated satellite navigation system of China. By the end of 2012, the regional BDS started to provide positioning, navigation, timing (PNT), and short message communication services for users throughout the Asia-Pacific region. As of June 2017, the current BDS constellation consists of five geostationary Earth orbit (GEO) satellites, six inclined geosynchronous orbit (IGSO) satellites and three medium Earth orbit (MEO) satellites. The BDS aims to build a global satellite navigation system consisting of 5 GEO, 3 IGSO, and 27 MEO satellites by 2020 (China Satellite Navigation Office (CSNO) 2012). The GLONASS constellation has been fully operated since October 2011 and has 24 satellites in orbit at present, offering a full global service (http://www.glonass-ianc.rsa.ru/en/GLONASS/). As of June 2017, 18 Galileo satellites are in orbit, but five of them are in abnormal state (E03 and E04 in the commissioning phase, E14 and E18 in incorrect orbital planes and E20 transmitting signal on one frequency), so only 13 Galileo satellites can operate to offer a continuous, flexible and precise positioning service and sub-services to a broad spectrum of users. As planned, Galileo will be completely deployed with 30 satellites by 2020 (http://www.esa.int/Our_Activities/Navigation/Galileo/What_is_Galileo).

With the rapid development of GNSS, the International GNSS Service (IGS) has initiated the Multi-GNSS Experiment (MGEX) program since 2012 (Montenbruck et al. 2014). The program aims to adapt to multi-frequency and multi-system satellite signals and to prepare a future, full-featured multi-GNSS service for the scientific community.

MGEX acquires and archives GNSS observation data but also committed to generate and disseminate GNSS data products, such as orbit and clock products (Rizos et al. 2013). At the present, 27 institutions of 16 countries participate in MGEX. Since 2012, more than 120 MGEX ground stations have been installed in parallel to the existing IGS stations. Several MGEX analysis centers are able to provide multi-GNSS precise orbit and clock products using MGEX and other tracking network data, as from the BeiDou Experimental Tracking Network (BETN), Cooperative Network for GIOVE Observations (CONGO). Up to now, seven MGEX analysis centers are committed to providing GNSS data products such as orbit and clocks, as shown in Table 1. In Table 1, the satellite systems "G", "R", "E", "C", and "J" represent the GPS, GLONASS, Galileo, BDS, and QZSS, respectively. These products are available from MGEX's official Web site (ftp://cddis.gsfc.nasa.gov/pub/gps/products/mgex) or other agencies' mirror ftps (ftp://igs.ensg.eu/pub/igs/Products/mgex).

Although remarkable progress has been achieved for GPS ambiguity resolution, GPS PPP still suffers from the problem of a long time to fix the first ambiguity (Geng et al. 2011). Multi-GNSS fusion can significantly shorten the PPP convergence time and improve the positioning accuracy (Li et al. 2015). Li et al. (2016) developed the GPS+BDS UPD estimation model and an initial analysis of the ambiguity resolved PPP with GPS and BDS was made. Results show that the TTFF of BDS-only AR is longer than 6 h and the success rate is less than 35% in general. For the combined GPS+BDS AR, the average TTFF has been shorten to 16.9 and 24.6 min in static and kinematic PPP mode, respectively. Liu et al. (2017a) estimated the BDS UPDs with a regional network and PPP AR was carried out at each station with a two-day dataset. Because of the FDMA strategy of GLONASS, GLONASS PPP faces difficulties due to existence of different wavelength and inter-frequency bias (IFB) among different satellites. To solve these problems, Liu et al. (2017b) estimated the GLONASS UPDs with a set of homogeneous receivers (Trimble NetR8) and performed the PPP AR with 12 stations of crustal movement

observation network of China (CMONOC). The positioning accuracy of GLONASS PPP has been improved from (1.42, 0.66, 1.55) to (0.39, 0.38, 1.39) cm for the east, north, and vertical components, respectively, within 2 h (Liu et al. 2017b). The fixing percentage for GPS alone is 11.70 and 46.8% within 5 and 10 min while 73.1 and 95.83% with GLONASS satellites added (Liu et al. 2017c). Geng and Bock (2016) proposed a general method where global ionosphere maps (GIM) are applied to GLONASS PPP to estimate UPDs with inhomogeneous receivers for PPP ambiguity resolution, which shows that hourly static GLONASS PPP AR can reach positioning accuracy of about 1 and 2 cm in RMS for the horizontal and vertical components, respectively. However, the modest accuracy of GIMs confines the PPP AR to an 800 km × 800 km area.

We will focus in this study on the UPD estimation based on GCRE four-system observation model to achieve the multi-GNSS PPP ambiguity resolution. The temporal and spatial characteristics of the UPD are analyzed and evaluated for all navigation satellite systems. The contribution of the multi-GNSS observations to the PPP ambiguity resolution is also investigated, and the performance of the GCRE-combined PPP AR is compared to that achieved with a single or dual constellation. Our paper is organized as follows: After this introduction, the multi-GNSS constellations and tracking networks are characterized in Sect. 2. In Sect. 3, the multi-GNSS observation model is formulated and the method to estimate four-system UPD is emphasized. In Sect. 4, we proposed a processing strategy for the Multi-GNSS PPP ambiguity resolution. In Sect. 5, we analyze the UPD results of the four different satellite systems. The performance of combined four-system PPP AR in terms of positioning accuracy, TTFF, and fixing percentage compared to the single-system and dual-system solutions is analyzed in Sect. 6. Finally, the conclusions and perspectives are provided in Sect. 7.

2 Multi-GNSS constellations and tracking network

2.1 Current GNSS constellations

The US American GPS and Russian GLONASS are both at full service status. GPS presently consists of 32 satellites distributed over 6 orbital planes. All satellites are at good condition except G04, which is unusable in most cases. Block IIA satellites were finally removed from the constellation in early 2016 after serving for almost two decades (Montenbruck et al. 2017). At the time of writing (June 2017), there are three generations of GPS satellites including Block IIR (12 satellites), Block IIR-M (7 satellites), and Block IIF (12 satellites). The new civil L2C signal and the aeronautical L5 signal are broadcast by the more recent generations of Block IIR-M (L2C) and IIF (L2C and L5) satellites.

China is constructing the BDS, and the deployment of BDS is divided into two phases: the regional system and the global system. BDS was the first system providing triple-frequency (known as B1-2, B2= E5a, B3) signals on all satellites. By the end of 2012, there were 14 BDS satellites (including 5 GEOs, 5 IGSOs, and 4 MEOs) deployed in orbit, making it possible to provide Asia-Pacific regional service. On March 30, 2015 the first new-generation BDS satellite (BDS-3) was launched (http://www.beidou.goc.cn), which means that China began to expand BDS from regional to a global coverage. By February 2016, five BDS-3 satellites (three MEOs and two IGSOs) have been launched. It is planned that BDS will become a global navigation satellites system providing stable and continuous service by 2020. As of June 2017, the BDS has presently 20 satellites in orbit, which includes 14 BDS-2 satellites (5 GEOs, 6 IGSOs, and 3 MEOs) providing healthy signals and valid navigation messages as well as 6 satellites (1 BDS-2 and 5 BDS-3 satellites) still in the phase of flight test.

The GLONASS constellation has been fully recovered since October 2011 and is operated with complete 24 satellites in orbits (http://www.glonass-ianc.rsa.ru/en/GLONASS/) as of mid 2017, enabling full global coverage. The constellation is mainly composed of GLONASS-M satellites, but already includes one modernized GLONASS-M+ and two GLONASS-K1 satellites (Montenbruck et al. 2017). The new GLONASS satellites support transmission of the new L3 code-division multiple-access (CDMA) signal (Urlichich et al. 2011).

The European Galileo system consists of two different generations of satellites namely IOV (In-Orbit Validation) and FOC (Full Operational Capability). Four IOV satellites were launched in 2011/2012. In May 2014, the IOV-FM4 satellite (E20) experienced a sudden power loss (de Selding 2014) and a permanent failure of the E5 and E6 signal transmission. On August 22, 2014, the first two FOC satellites (E14 and E18) were launched but they were injected into wrong orbits and are assigned a "testing" status on the constellation information page (https://www.gsc-europa.eu/system-status/Constellation-Information). However, they can still be used for the original purpose because they can offer proper navigation signals and broadcast navigation messages. On December 15, 2016, initial open services of the Galileo system were declared by the European Union. By now, 13 Galileo satellites can be observed including 3 IOV and 10 FOC satellites. The fully deployed Galileo system is scheduled to be accomplished in 2020 and will consist of 24 operational satellites plus six in-orbit spares, positioned in three circular MEO planes at 23222 km altitude above the Earth (http://www.esa.int/Our_Activities/Navigation/The_future_-_Galileo/What_is_Galileo). Table 2

Table 2 Deployment status of current multi-GNSS as of June 2017

System	Blocks	Signals	Sats
GPS	IIR	L1 C/A, L1/L2 P(Y)	12
	IIR-M	L1 C/A, L1/L2 P(Y), L2C, L1/L2 M	7
	IIF	L1 C/A, L1/L2 P(Y), L2C, L1/L2 M, L5	12
GLONASS	M	L1/L2 C/A & P	23
	M+	L1/L2 C/A & P, L3	1
	K	L1/L2 C/A & P, L3	2
BDS-2	GEO	B1-2, B2, B3	6
	IGSO	B1-2, B2, B3	6
	MEO	B1-2, B2, B3	3
BDS-3	IGSO	B1-2, B1, B2, B3ab	2
	MEO	B1-2, B1, B2, B3ab	3
Galileo	IOC	E1, E6, E5a/b/ab	4
	FOC	E1, E6, E5a/b/ab	10(+4)

Numbers in brackets refer to satellites that have not yet been declared operational or offer restricted functionality

summarizes the current deployment status of multi-GNSS constellations in terms of satellite types, transmitted signals, and available satellite numbers.

2.2 Available GNSS ground tracking networks

The International GNSS Service (IGS) has initiated the Multi-GNSS Experiment (MGEX) in response to the new navigation satellites systems and their signals. A new network of multi-GNSS monitoring stations, as a backbone of the MGEX project, has been deployed around the globe in parallel to the legacy IGS network for GPS and GLONASS. All MGEX stations support at least one among the BDS, Galileo or QZSS systems besides GPS, while most of MGEX stations can track GLONASS satellites. By mid-2015, all MGEX stations were formally reviewed for conformity with established IGS site guidelines (http://kb.igs.org/hc/en-us/article_attachments/202277487/IGS_Site_Guidelines_July_2015.pdf). All previous MGEX stations with only few exceptions were fully incorporated into the official IGS network in 2016 (Montenbruck et al. 2017). By June 2017, the IGS multi-GNSS network has grown to 188 stations (http://www.igs.org/network), as shown in Fig. 1. Galileo satellites are tracked by about 180 stations, and about 140 stations are tracking the BDS satellites. However, from CDDIS (ftp://cddis.gsfc.nasa.gov/), only 67 stations with BDS observations can be found, as shown in Fig. 2 (in *blue circles*). These stations are mainly located in European and Asian-Pacific region.

The BDS signals can also be tracked by Chinese tracking networks, such as the Crustal Movement Observation Network of China (CMONOC) and Continuously Operating Reference Stations (CORS) network. In order to monitor crustal movement and gravity change, China has established a continuous nationwide observation network since 2012, called CMONOC. CMONOC is composed of 260 continuous GNSS observation stations and 2000 irregular GNSS observation station. A network of 18 stations with BDS observations from CMONOC (in *violet triangles* in Fig. 2, *left* panel) is used to estimate BDS UPDs in our study. Besides the above-mentioned networks, a local Hong Kong CORS network with 18 BDS-enabled stations (the *red triangles* in Fig. 2, *right* panel) is also employed in this study. Three sets of BDS UPDs are estimated based on data from the three BDS networks of different spatial scales in Fig. 2 and their difference will be analyzed in Sect. 5.

As for the estimation of GPS, GLONASS, and Galileo UPDs, different networks are applied for different constellations. Most stations of the basic IGS network can track both GPS and GLONASS satellites, and some can even track Galileo. So in the estimation of GPS, GLONASS and Galileo UPDs, mixture networks consisting of MGEX/IGS stations are chosen. Note that GLONASS networks must be grouped by stations equipped with homogeneous receivers since inhomogeneous receivers may have different IFBs.
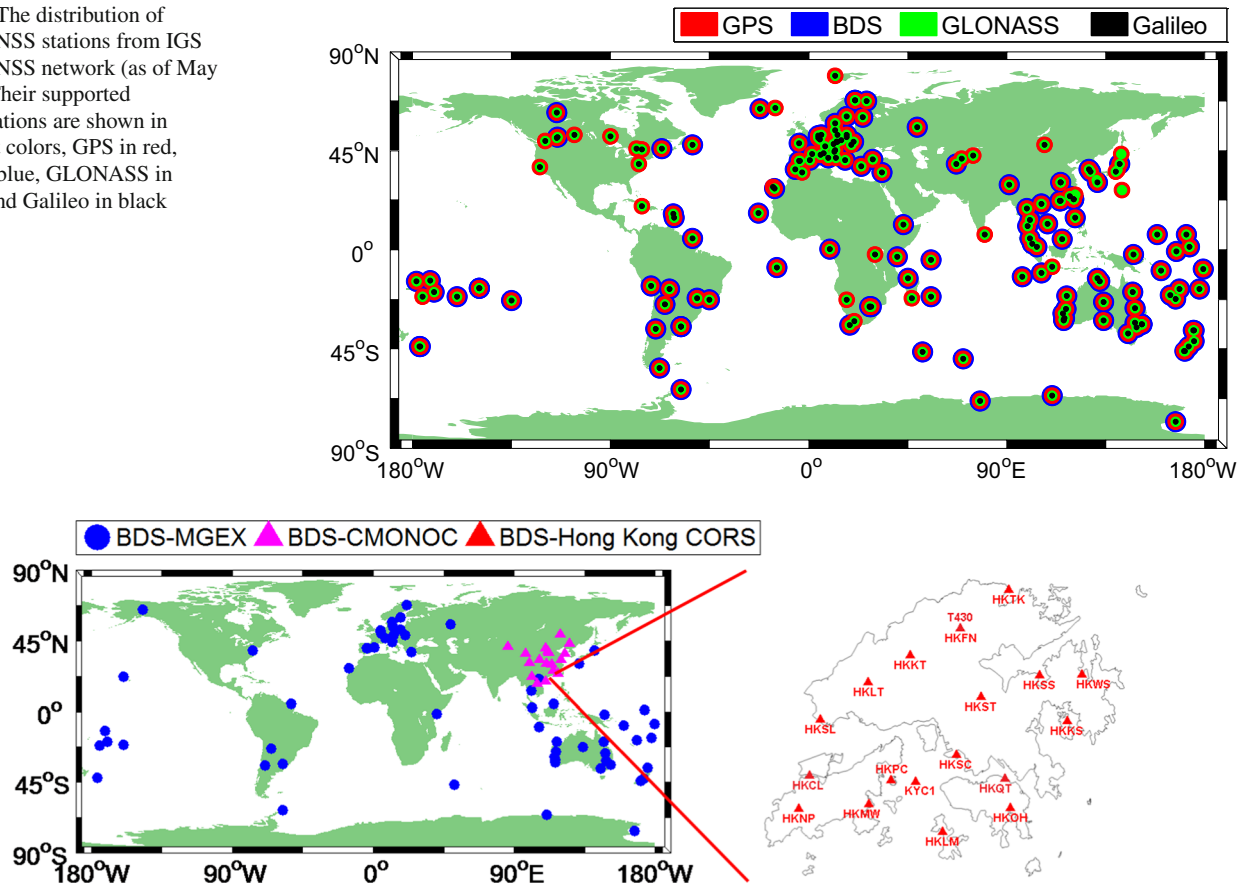
3 Multi-GNSS UPD estimation

The GNSS phase $L_{r,j}^s$ and pseudorange $P_{r,j}^s$ observation equations at a particular epoch can be expressed as following (Hofmann-Wellenhof et al. 2008; Li et al. 2015),

$$L_{r,j}^s = \rho_{r\,g}^s + c(t_r - t^s) + \lambda_j(B_{r,j} - B_j^s) + \lambda_j N_{r,j}^s$$
$$- I_{r,j}^s + T_r^s + \varepsilon_{r,j}^s \tag{1}$$
$$P_{r,j}^s = \rho_{r\,g}^s + c(t_r - t^s) + c(b_{r,j} - b_j^s) + I_{r,j}^s + T_r^s + e_{r,j}^s \tag{2}$$

Fig. 2 Three GNSS ground networks with BDS observations. In the left panel, the blue circles denote 67 stations from the MGEX network, and the violet triangles denote 18 stations from the CMONOC network. The red triangles in the right panel denote 18 stations from the Hong Kong CORS network

where s, r and j refer to satellite, receiver, and frequency, respectively; λ_j is the wavelength of frequency j in meters; t^s and t_r are the clock offsets of satellite and receiver in seconds; $N_{r,j}^s$ refers to the integer ambiguity in cycles; $B_{r,j}$ and B_j^s are the phase delay of receiver and satellite in cycles; $b_{r,j}$ and b_j^s are the code hardware delay of receiver and satellite in seconds, respectively; the ionospheric delays $I_{r,j}^s$ in meters at different frequencies can be expressed as $I_{r,j}^s = \kappa_j \cdot I_{r,1}^s$, $\kappa_j = \lambda_j^2/\lambda_1^2$; T_r^s is the slant tropospheric delay in meters; $e_{r,j}^s$ and $\varepsilon_{r,j}^s$ denote the sum of measurement noise and multipath error for the code and carrier phase observations; ρ_g denotes the geometric distance from satellite to receiver. The phase center offsets (PCOs) and variations (PCVs), tidal loading and phase windup can be corrected according to the existing models (Kouba 2009).

To eliminate the first-order ionospheric delays of the code and carrier phase observations, ionosphere-free (IF) combination is usually used to estimate the PPP parameters. Starting from the basic observables as described previously,

the GNSS phase and code IF combinations ($L_{r,\mathrm{IF}}^s$ and $P_{r,\mathrm{IF}}^s$) can be defined as:

$$L_{r,\mathrm{IF}}^s = \frac{f_i^2}{f_i^2 - f_j^2} L_{r,i}^s - \frac{f_j^2}{f_i^2 - f_j^2} L_{r,j}^s \tag{3}$$

$$P_{r,\mathrm{IF}}^s = \frac{f_i^2}{f_i^2 - f_j^2} P_{r,i}^s - \frac{f_j^2}{f_i^2 - f_j^2} P_{r,j}^s \tag{4}$$

where i and j indicate different frequency of code and phase measurements; f_i and f_j are the carrier frequency of $L_{r,i}$ and $L_{r,j}$, respectively. The multi-frequency measurements allow various IF combinations to be computed from the different pairs. In our study, we calculated the IF combination using observations on frequencies L1 and L2 for GPS and GLONASS, B1 and B2 for BDS, E1 and E5a for Galileo. Under the multi-constellation environment, the GCRE IF combination model of code and carrier phase observations can be formulated as:

$$
\begin{cases}
P_{r,\text{IF}}^{G} = \rho_{r\,g}^{G} + c(t_r - t^{G}) + c(b_{r,\text{IF}}^{G} - b_{\text{IF}}^{s,G}) + T_r^{G} + e_{r,\text{IF}}^{G} \\
P_{r,\text{IF}}^{C} = \rho_{r\,g}^{C} + c(t_r - t^{C}) + c(b_{r,\text{IF}}^{C} - b_{\text{IF}}^{s,C}) + T_r^{C} + e_{r,\text{IF}}^{C} \\
P_{r,\text{IF}}^{R_k} = \rho_{r\,g}^{R_k} + c(t_r - t^{R_k}) + c(b_{r,\text{IF}}^{R_k} - b_{\text{IF}}^{s,R_k}) + T_r^{R_k} + e_{r,\text{IF}}^{R_k} \\
P_{r,\text{IF}}^{E} = \rho_{r\,g}^{E} + c(t_r - t^{E}) + c(b_{r,\text{IF}}^{E} - b_{\text{IF}}^{s,E}) + T_r^{E} + e_{r,\text{IF}}^{E}
\end{cases}
\tag{5}
$$

$$
\begin{cases}
L_{r,\text{IF}}^{G} = \rho_{r\,g}^{G} + c(t_r - t^{G}) + \lambda_{\text{IF},G}(N_{r,\text{IF}}^{G} + B_{r,\text{IF}}^{G} - B_{\text{IF}}^{s,G}) + T_r^{G} + \varepsilon_{r,\text{IF}}^{G} \\
L_{r,\text{IF}}^{C} = \rho_{r\,g}^{C} + c(t_r - t^{C}) + \lambda_{\text{IF},C}(N_{r,\text{IF}}^{C} + B_{r,\text{IF}}^{C} - B_{\text{IF}}^{s,C}) + T_r^{C} + \varepsilon_{r,\text{IF}}^{C} \\
L_{r,\text{IF}}^{R_k} = \rho_{r\,g}^{R_k} + c(t_r - t^{R_k}) + \lambda_{\text{IF},R_k}(N_{r,\text{IF}}^{R_k} + B_{r,\text{IF}}^{R_k} - B_{\text{IF}}^{s,R_k}) + T_r^{R_k} + \varepsilon_{r,\text{IF}}^{R_k} \\
L_{r,\text{IF}}^{E} = \rho_{r\,g}^{E} + c(t_r - t^{E}) + \lambda_{\text{IF},E}(N_{r,\text{IF}}^{E} + B_{r,\text{IF}}^{E} - B_{\text{IF}}^{s,E}) + T_r^{E} + \varepsilon_{r,\text{IF}}^{E}
\end{cases}
\tag{6}
$$

where the superscripts G, C, R, and E refer to the GPS, BDS, GLONASS and Galileo satellites, respectively; R_k denotes the GLONASS satellite with frequency factor k; λ_{IF} is the wavelength of the IF carrier phase; $b_{r,\text{IF}}$ and b_{IF}^{s} are IF code hardware delay of receiver and satellite signal; $N_{r,\text{IF}}$ is the carrier phase IF ambiguity; $B_{r,\text{IF}}$ and B_{IF}^{s} are the IF receiver-dependent and satellite-dependent phase delay, respectively; $e_{r,\text{IF}}^{s}$ and $\varepsilon_{r,\text{IF}}$ denote the sum of measurement noise and multipath error of the IF combination, respectively. Due to the different frequencies and signal structure of the individual GNSS, the IF code hardware delays $b_{r,\text{IF}}^{G}$, $b_{r,\text{IF}}^{R_k}$, $b_{r,\text{IF}}^{E}$ and $b_{r,\text{IF}}^{C}$ are different in one multi-GNSS receiver. And the dif-

Multi-GNSS precise orbit and clock from GFZ are used for four-system ambiguity-float PPP (Uhlemann et al. 2015). Since precise satellite clocks are determined by IF combination observation data from a global GNSS ground tracking network, the code IF hardware delay at the satellite side can be assimilated into the satellite clock product of MGEX. It is worthwhile to note that the ISB/IFB parameters need to be introduced for each system and each frequency for GLONASS while GPS is selected as reference in the multi-GNSS PPP processing. Because the code and carrier phase share the same receiver clock, the re-parameterized ambiguity of four systems can be expressed as the integer ambiguities and their UPDs:

$$
\begin{cases}
\bar{N}_{r,\text{IF}}^{G} = N_{r,\text{IF}}^{G} + d_{r,\text{IF}}^{G} - d_{\text{IF}}^{s,G} = N_{r,\text{IF}}^{G} + B_{r,\text{IF}}^{G} - B_{\text{IF}}^{s,G} - \dfrac{c(b_{r,\text{IF}}^{G} - b_{\text{IF}}^{s,G})}{\lambda_{\text{IF},G}} \\
\bar{N}_{r,\text{IF}}^{C} = N_{r,\text{IF}}^{C} + d_{r,\text{IF}}^{C} - d_{\text{IF}}^{s,C} = N_{r,\text{IF}}^{C} + B_{r,\text{IF}}^{C} - B_{\text{IF}}^{s,C} - \dfrac{c(b_{r,\text{IF}}^{C} - b_{\text{IF}}^{s,C})}{\lambda_{\text{IF},C}} \\
\bar{N}_{r,\text{IF}}^{R_k} = N_{r,\text{IF}}^{R_k} + d_{r,\text{IF}}^{R_0} - d_{\text{IF}}^{s,R_k} + \left(F_{\text{IF}}^{R_k} - \dfrac{H_{\text{IF}}^{R_k}}{\lambda_{\text{IF},R_k}}\right) = N_{r,\text{IF}}^{R_k} + B_{r,\text{IF}}^{R_0} - B_{\text{IF}}^{s,R_k} + F_{\text{IF}}^{R_k} - \dfrac{c(b_{r,\text{IF}}^{R_0} - b_{\text{IF}}^{s,R_k}) + H_{\text{IF}}^{R_k}}{\lambda_{\text{IF},R_k}} \\
\bar{N}_{r,\text{IF}}^{E} = N_{r,\text{IF}}^{E} + d_{r,\text{IF}}^{E} - d_{\text{IF}}^{s,E} = N_{r,\text{IF}}^{E} + B_{r,\text{IF}}^{E} - B_{\text{IF}}^{s,E} - \dfrac{c(b_{r,\text{IF}}^{E} - b_{\text{IF}}^{s,E})}{\lambda_{\text{IF},E}}
\end{cases}
\tag{7}
$$

ferences are called inter-system biases (ISB). Similarly, the phase delays $B_{r,\text{IF}}^{G}$, $B_{r,\text{IF}}^{R_k}$, $B_{r,\text{IF}}^{E}$ and $B_{r,\text{IF}}^{C}$ are also different and their difference are ISB for phase delays. For the GLONASS satellites with different frequency factors, the receiver code hardware delay $b_{r,\text{IF}}^{R_k}$ as well as the phase delay $B_{r,\text{IF}}^{R_k}$ are different and are usually called inter-frequency biases (IFB). The receiver IFB is not separable with the receiver clock and we thus further define the IFB of each satellite as the difference with respect to a particular satellite.

where $\bar{N}_{r,\text{IF}}^{G}$, $\bar{N}_{r,\text{IF}}^{R_k}$, $\bar{N}_{r,\text{IF}}^{E}$ and $\bar{N}_{r,\text{IF}}^{C}$ are float IF ambiguities for multi-GNSS systems; For GPS, BDS and Galileo, $d_{r,\text{IF}}$ is the receiver UPDs, which is the linear combination of IF code hardware delay and phase delay, with $d_{r,\text{IF}} = B_{r,\text{IF}} - \frac{c \cdot b_{r,\text{IF}}}{\lambda_{\text{IF}}}$, and the satellite UPDs d_{IF}^{s} is the linear combination of IF code hardware delay and phase delay at satellite side, which can be expressed as $d_{\text{IF}}^{s} = B_{\text{IF}}^{s} - \frac{c \cdot b_{\text{IF}}^{s}}{\lambda_{\text{IF}}}$; As for GLONASS, we define the code IFB $H_{\text{IF}}^{R_k}$ and phase IFB $F_{\text{IF}}^{R_k}$ of each satellite as the difference with respect to the reference satellite R_0; $d_{r,\text{IF}}^{R_0}$ and d_{IF}^{s,R_k} are the UPDs at receiver and satellite side, with $d_{r,\text{IF}}^{R_0} = B_{r,\text{IF}}^{R_0} - \frac{c \cdot b_{r,\text{IF}}^{R_0}}{\lambda_{\text{IF},R_0}}$ and $d_{\text{IF}}^{s,R_k} = B_{\text{IF}}^{s,R_k} - \frac{c \cdot b_{\text{IF}}^{s,R_k}}{\lambda_{\text{IF},R_k}}$. The

code hardware delay and phase delay are not separable from the ambiguities of each system. Besides the code hardware delay and phase delay, the code and carrier IFBs are also absorbed in the ambiguities of GLONASS.

For an ambiguity-fixed PPP solution, $N_{r,\text{IF}}$ is usually expressed as the combination of the narrow-lane (NL) ambiguity and integer wide-lane (WL) ambiguity. The WL ambiguity can be derived with the Hatch–Melbourne–Wübbena (HMW) (Hatch 1982; Melbourne 1985; Wübbena 1985) combination of the carrier phase and code observations as

$$\bar{N}_{r,\text{wl}}^{G} = \left(\frac{L_{r,1}^{G}}{\lambda_1^{G}} - \frac{L_{r,2}^{G}}{\lambda_2^{G}} - \frac{f_1^{G} P_{r,1}^{G} + f_2^{G} P_{r,2}^{G}}{(f_1^{G} + f_2^{G})\lambda_{\text{wl}}^{G}} \right)$$
$$= N_{r,\text{wl}}^{G} + d_{r,\text{wl}}^{G} - d_{\text{wl}}^{s,G} \qquad (8)$$

$$\bar{N}_{r,\text{wl}}^{C} = \left(\frac{L_{r,1}^{C}}{\lambda_1^{C}} - \frac{L_{r,2}^{C}}{\lambda_2^{C}} - \frac{f_1^{C} P_{r,1}^{C} + f_2^{C} P_{r,2}^{C}}{(f_1^{C} + f_2^{C})\lambda_{\text{wl}}^{C}} \right)$$
$$= N_{r,\text{wl}}^{C} + d_{r,\text{wl}}^{C} - d_{\text{wl}}^{s,C} + \text{CB}_{\text{wl}}^{s,C} \qquad (9)$$

$$\bar{N}_{r,\text{wl}}^{R_k} = \left(\frac{L_{r,1}^{R_k}}{\lambda_1^{R_k}} - \frac{L_{r,2}^{R_k}}{\lambda_2^{R_k}} - \frac{f_1^{R_k} P_{r,1}^{R_k} + f_2^{R_k} P_{r,2}^{R_k}}{(f_1^{R_k} + f_2^{R_k})\lambda_{\text{wl}}^{R_k}} \right)$$
$$= N_{r,\text{wl}}^{R_k} + d_{r,\text{wl}}^{R_0} - d_{\text{wl}}^{s,R_k} + \frac{H_{r,\text{wl}}^{R_k}}{\lambda_{\text{wl}}^{R_k}} + F_{r,\text{wl}}^{R_k} \qquad (10)$$

$$\bar{N}_{r,\text{wl}}^{E} = \left(\frac{L_{r,1}^{E}}{\lambda_1^{E}} - \frac{L_{r,2}^{E}}{\lambda_2^{E}} - \frac{f_1^{E} P_{r,1}^{E} + f_2^{E} P_{r,2}^{E}}{(f_1^{E} + f_2^{E})\lambda_{\text{wl}}^{E}} \right)$$
$$= N_{r,\text{wl}}^{E} + d_{r,\text{wl}}^{E} - d_{\text{wl}}^{s,E} \qquad (11)$$

with

$$d_{r,\text{wl}} = \frac{B_{r,1}}{\lambda_1} - \frac{B_{r,2}}{\lambda_2} - \frac{f_1 b_{r,1} + f_2 b_{r,2}}{(f_1 + f_2)\lambda_{\text{wl}}} \qquad (12)$$

$$d_{\text{wl}}^{S} = \frac{B_1^{S}}{\lambda_1} - \frac{B_2^{S}}{\lambda_2} - \frac{f_1 b_1^{S} + f_2 b_2^{S}}{(f_1 + f_2)\lambda_{\text{wl}}} \qquad (13)$$

$$H_{r,\text{wl}}^{R_k} = -\frac{f_1^{R_k} H_{r,1}^{R_k} + f_2^{R_k} H_{r,2}^{R_k}}{(f_1^{R_k} + f_2^{R_k})} \qquad (14)$$

$$F_{r,\text{wl}}^{R_k} = \frac{F_{r,1}^{R_k}}{\lambda_1^{R_k}} - \frac{F_{r,2}^{R_k}}{\lambda_2^{R_k}} \qquad (15)$$

where $\bar{N}_{r,\text{wl}}$ and $N_{r,\text{wl}}$ are the float and integer WL ambiguities with corresponding wavelength λ_{wl}^{k}; f_1 and f_2 are the carrier frequency of $L_{r,1}$ and $L_{r,2}$, respectively; $d_{r,\text{wl}}$ and d_{wl}^{s} are the receiver and satellite WL UPDs; $\text{CB}_{\text{wl}}^{s,C}$ refers to the BDS satellite-induced code bias; $H_{r,\text{wl}}^{R_k}$ and $F_{r,\text{wl}}^{R_k}$ denote the code and phase WL IFB for GLONASS satellites, respectively.

The satellite-induced code bias ($\text{CB}_{\text{wl}}^{s,C}$) was identified to exist in BDS code observations, which affects the precision and consistence of the WL ambiguity derived from MW combination. For IGSO and MEO satellites, the variation of this error reveals elevation-dependent and can be corrected with empirical correction model (Wanninger and Beer 2015). However, it is impossible to use elevation-dependent correction model to correct the code bias of GEO satellites because the elevation of GEO satellites stays relatively static position to observer. Besides the satellite-induced code bias, the GEO observations are also affected by the multipath of the station seriously. To mitigate the effect of satellite-induced code bias and multipath of GEO observations, the wavelet filter is used to extract the systematic variation superimposed in code observation and apply it back as correction (Wang et al. 2015). It is worthwhile noting that the regional network will get a better result than that of global network for WL UPDs since the satellite-induced code biases are almost the same for all tracking stations and then will be absorbed into the WL UPDs at satellite side.

With the fixed WL ambiguities, the float NL ambiguities can be derived from IF ambiguities according to Eq. 16 (for the sake of simplicity, the symbol denoting the satellite system is not given here).

$$\lambda_{\text{nl}} \cdot \bar{N}_{r,\text{nl}} = \lambda_{\text{IF}} \cdot \bar{N}_{r,\text{IF}} - \frac{cf_2}{f_1^2 - f_2^2} \cdot N_{r,\text{wl}} \qquad (16)$$

where λ_{nl} and λ_{IF} are wavelength of NL ambiguity ($N_{r,\text{nl}}$) and IF ambiguity (N_{IF}).

BDS has currently (as of mid 2017) a better coverage in the Asia-Pacific area than other regions. More than seven satellites in parallel can be tracked by the stations in the Asia-Pacific area. However, the number of available BDS satellites is still quite limited (usually fewer than 4) in other regions. Similarly, some European stations can track 3–5 Galileo satellites while in other region areas only 2–3 satellites can be tracked, which cannot contribute to the NL UPD estimation in single-system PPP. To overcome the limitation of the visible satellites for BDS and Galileo, the GCRE-combined PPP float solutions were performed firstly to generate the four-system ambiguities and then the UPDs of four systems can be estimated from these precise ambiguities. The use of the multi-GNSS constellation can significantly increase the number of visible satellite and the ambiguities of each system can be precisely estimated in multi-GNSS PPP.

For BDS, the quality of GEO NL UPDs is affected by the low precision of the orbits. The float NL ambiguity of a particular GEO satellite C_0 for n stations can be expressed as:

$$\bar{N}_{1,\text{nl}}^{C_0} = N_{1,\text{nl}}^{C_0} + d_{1,\text{nl}}^{C_0} - d_{\text{nl}}^{s,C_0} + O_{1,\text{nl}}^{C_0}$$
$$\bar{N}_{2,\text{nl}}^{C_0} = N_{2,\text{nl}}^{C_0} + d_{2,\text{nl}}^{C_0} - d_{\text{nl}}^{s,C_0} + O_{2,\text{nl}}^{C_0}$$
$$\bar{N}_{3,\text{nl}}^{C_0} = N_{3,\text{nl}}^{C_0} + d_{3,\text{nl}}^{C_0} - d_{\text{nl}}^{s,C_0} + O_{3,\text{nl}}^{C_0}$$

$$\vdots$$

$$\bar{N}_{n,\text{nl}}^{C_0} = N_{n,\text{nl}}^{C_0} + d_{n,\text{nl}}^{C_0} - d_{\text{nl}}^{s,C_0} + O_{n,\text{nl}}^{C_0} \tag{17}$$

where $O_{i,\text{nl}}^{C_0}$ is orbit error of the GEO satellite at i station. In order to overcome the limitation of the orbit error, the regional network will be used to estimate the UPDs. Since the network is small, the orbit error $O_{i,\text{nl}}^{C_0}$ in a particular satellite C_0 is similar for different stations and can be absorbed in to the NL satellite UPDs (d_{nl}^{s,C_0}).

For GLONASS, both WL and NL ambiguities are affected by the code and carrier phase IFBs which depend on the satellite and receiver. The WL and NL IFBs of a particular satellite are different for inhomogeneous receiver. The carrier phase IFB can be modeled as the linear function of frequency and the correction model are applied to calibrate phase IFB (Wanninger 2012). However, the code IFB cannot be calibrated by a general model in that one correction model of one receiver type cannot be applied to other types (Yamada et al. 2010). If the code or carrier phase IFB is not calibrated, neither the UPD estimation nor the ambiguity resolution can be achieved (Reussner and Wanninger 2011). To eliminate the effect of the IFBs on the GLONASS UPD estimation, we estimate the WL and NL UPDs using homogeneous receivers. Therefore, the code and carrier phase IFB for a particular satellite will be the same for all involved receivers and thus can be absorbed into the satellite UPDs (Liu et al. 2017b). Taking the WL ambiguity as an example, Eq. 10 is written as:

$$\bar{N}_{r,\text{wl}}^{R_k} = N_{r,\text{wl}}^{R_k} + d_{r,\text{wl}}^{R_0} - \bar{d}_{\text{wl}}^{s,R_k} \tag{18}$$

with

$$\bar{d}_{\text{wl}}^{s,R_k} = d_{\text{wl}}^{s,R_k} - \frac{H_{r,\text{wl}}^{R_k}}{\lambda_{\text{wl}}^{R_k}} - F_{r,\text{wl}}^{R_k} \tag{19}$$

With the above reformulation, the GLONASS UPDs estimation will not be affected by the IFBs.

Here we proposed a four-system undifferenced UPD estimation method to generate the WL and NL UPD values epoch by epoch. The undifferenced WL and NL ambiguities, which are derived from HMW combination and IF combination can be further describe as:

$$D_r^{G_k} = \bar{N}_i^{G_k} - N_i^{G_k} = d_G - d^{G_k} \tag{20}$$

$$D_r^{C_k} = \bar{N}_i^{C_k} - N_i^{C_k} = d_C - d^{C_k} \tag{21}$$

$$D_r^{R_k} = \bar{N}_i^{R_k} - N_i^{R_k} = d_R - d^{R_k} \tag{22}$$

$$D_r^{E_k} = \bar{N}_i^{E_k} - N_i^{E_k} = d_E - d^{E_k} \tag{23}$$

where d_G, d_R, d_E and d_C are receiver UPDs of different system in one multi-GNSS receiver while $d^{G_k}, d^{E_k}, d^{C_k}$ and d^{R_k} denote the satellite UPD of the GPS, GLONASS, Galileo and BDS satellites, respectively; $D_r^{G_k}, D_r^{C_k}, D_r^{R_k}$ and $D_r^{E_k}$ denote the combined UPDs of satellite k of particular constellation and receiver r.

Assuming the number of stations is n and m satellites are available in every station, the equations for UPD estimation of GPS, BDS, GLONASS and Galileo can be formulated in matrix form as following (Li et al. 2013):

$$\begin{bmatrix} D_1^1 \\ \vdots \\ D_1^m \\ D_2^1 \\ \vdots \\ D_2^m \\ \vdots \\ D_n^1 \\ \vdots \\ D_n^m \end{bmatrix} = \begin{bmatrix} R_{1G} & R_{1C} & R_{1R} & R_{1E} & s_1 \\ R_{2G} & R_{2C} & R_{2R} & R_{2E} & s_2 \\ \vdots & \vdots & \vdots & \vdots & \vdots \\ R_{nG} & R_{nC} & R_{nR} & R_{nE} & s_n \end{bmatrix} \cdot \begin{bmatrix} d_G \\ d_C \\ d_R \\ d_E \\ d^s \end{bmatrix} \tag{24}$$

where R_{iG}, R_{iC}, R_{iR} and R_{iE} are the coefficient matrices for the receiver UPDs of different satellite systems. In matrix R_i, the elements of one column corresponding to receiver UPD of particular system are 1 while the elements of other columns are 0; d^s is the satellite UPD vector; s_i is the coefficient matrix of satellite UPDs d^s. In matrix s_i, the coefficient of satellite UPD is -1 while the other elements are 0.

The UPDs of a single receiver for different systems are set as different parameters for estimation because of the different signal frequencies and receiver processing paths for observations from different systems. To eliminate the rank-deficiency for multi-GNSS UPD estimation equation, one station or one satellite is selected as the datum for each individual satellite system with the corresponding UPD set as zero. Then UPDs values can be estimated in iterative way (see Eq. 24) epoch by epoch. Before the iterative UPD estimation, the initial UPDs are estimated. We assumed that the UPD of the station with the largest number of tracked satellites is zero, and the nearest integers of the ambiguities at this station are integer ambiguities and the fractional part is regarded as estimated satellite UPD. For the next station with common satellites, the ambiguities corrected by estimated satellite UPDs should have close fractional parts. Therefore, the mean fractional part of all the common satellites will give a better estimate of UPD at this station using the formulation of Gabor and Nerem (1999) to avoid the fractional part biased by ± 1 cycle. Then, the other satellite UPDs of this station are obtained by removing the receiver UPD from the fraction part of the ambiguity. One can estimate the satellite UPDs by averaging the satellite UPDs of each station which can track this satellite. Repeating this procedure for all satellites and all stations, all satellite UPDs and receiver

UPDs can be obtained as the prior values of UPDs. In the process of the iteration, the estimated UPDs are applied to correct the undifferenced ambiguities, the corrected ambiguities with a fraction part over a threshold of 0.25 cycles will not contribute to estimate the UPD at next iterative step. The Detection, Identification and Adaptation (DIA) quality control procedure is also used to reject the outliers (Teunissen 1990; Li et al. 2013). This iteration stops when the UPDs of adjacent iterative results are close enough, and the UPDs from the last iteration are provided for the user side.

4 Multi-GNSS PPP ambiguity resolution

With the estimated multi-GNSS WL and NL UPD products, the integer property of WL and NL ambiguity will be recovered and then the ambiguities can be fixed to integers at a user side. The multi-GNSS ambiguities are lumped together, which will offer abundant float ambiguities to be fixed. The rounding strategy (Dong and Bock 1989; Ge et al. 2008) is applied to fix the WL ambiguities while a search strategy based on the LAMBDA (Teunissen 1995) method is used to search for the optimal integer solution of NL ambiguity. In theory, with the plenty of float ambiguity, more ambiguities will contribute to a better result of PPP AR. However, in some cases, some ambiguities may not be sufficiently precise to resolve the all integer ambiguities with a sufficiently high success rate. Therefore, the partially fixed integer solution is applied to select the high quality ambiguities with fixed priority, such as the ambiguities at high elevation angle and with high precision of float solutions (Teunissen et al. 1999; Li and Zhang 2015). The ratio test will be used to validate the ambiguity validation with a threshold of 2 (Han 1997).

4.1 WL ambiguity fixing

Before the multi-GNSS WL ambiguity fixing, it is necessary to correct the BDS satellite-induced code bias firstly since such variations can result in code-phase divergences of more than 1 m. The code bias of GEO satellite needs to be corrected by the wavelet filter while that of IGSO and MEO satellite can be corrected with empirical correction model of Wanninger and Beer (2015). If the UPD product is estimated by the small regional network, the GEO code bias can be ignored since the code biases are assimilated by the satellite UPDs. Similarly, for GLONASS, the code and carrier phase IFB can be neglected for ambiguity resolution since the IFBs are absorbed by the satellite UPDs.

To fix the WL ambiguity, the float WL ambiguities of four systems derived from HMW combination were corrected by the WL satellite UPDs firstly, as shown in the principle of (25)–(28):

$$\hat{N}_{r,\mathrm{wl}}^{G_k} = \bar{N}_{r,\mathrm{wl}}^{G_k} - d_{\mathrm{wl}}^{s,G_k}, \quad \sigma_{\hat{N}_{r,\mathrm{wl}}^{G_k}}^2 = \sigma_{\bar{N}_{\mathrm{wl},i}^{Gj}}^2 + \sigma_{b_{\mathrm{wl}}^{s,Gj}}^2 \quad (25)$$

$$\hat{N}_{r,\mathrm{wl}}^{C_k} = \bar{N}_{r,\mathrm{wl}}^{C_k} - d_{\mathrm{wl}}^{s,C_k}, \quad \sigma_{\hat{N}_{r,\mathrm{wl}}^{C_k}}^2 = \sigma_{\bar{N}_{\mathrm{wl},i}^{Cj}}^2 + \sigma_{b_{\mathrm{wl}}^{s,Cj}}^2 \quad (26)$$

$$\hat{N}_{r,\mathrm{wl}}^{R_k} = \bar{N}_{r,\mathrm{wl}}^{R_k} - d_{\mathrm{wl}}^{s,R_k}, \quad \sigma_{\hat{N}_{r,\mathrm{wl}}^{R_k}}^2 = \sigma_{\bar{N}_{\mathrm{wl},i}^{Rj}}^2 + \sigma_{b_{\mathrm{wl}}^{s,Rj}}^2 \quad (27)$$

$$\hat{N}_{r,\mathrm{wl}}^{E_k} = \bar{N}_{r,\mathrm{wl}}^{E_k} - d_{\mathrm{wl}}^{s,E_k}, \quad \sigma_{\hat{N}_{r,\mathrm{wl}}^{E_k}}^2 = \sigma_{\bar{N}_{\mathrm{wl},i}^{Ej}}^2 + \sigma_{b_{\mathrm{wl}}^{s,Ej}}^2 \quad (28)$$

where $\bar{N}_{r,\mathrm{wl}}$ and $\sigma_{\bar{N}_{r,\mathrm{wl}}}^2$ denote the undifferenced float WL ambiguity and its variance; $\hat{N}_{r,\mathrm{wl}}$ refer to WL ambiguity with satellite UPDs corrected.

The receiver WL UPD ($d_{r,\mathrm{wl}}$) can be obtained by averaging the fractional parts of all the available WL ambiguities. However, the average value is not a trivial result of receiver UPD and the fractional part can be biased by ± 1 cycle, which means -0.2 cycles can be described as 0.8 cycles. Gabor and Nerem (1999) proposed a formulation to solve this problem, which reads:

$$d_{r,\mathrm{wl}}^G = \mathrm{atan2}\left(\frac{\sum_{k=1}^{n_G} \cos(\hat{N}_{r,\mathrm{wl}}^{G_k} 2\pi)}{n_G}, \frac{\sum_{k=1}^{n_G} \sin(\hat{N}_{r,\mathrm{wl}}^{G_k} 2\pi)}{n_G}\right)/2\pi \quad (29)$$

$$d_{r,\mathrm{wl}}^C = \mathrm{atan2}\left(\frac{\sum_{k=1}^{n_C} \cos(\hat{N}_{r,\mathrm{wl}}^{C_k} 2\pi)}{n_C}, \frac{\sum_{k=1}^{n_G} \sin(\hat{N}_{r,\mathrm{wl}}^{C_k} 2\pi)}{n_C}\right)/2\pi \quad (30)$$

$$d_{r,\mathrm{wl}}^R = \mathrm{atan2}\left(\frac{\sum_{k=1}^{n_R} \cos(\hat{N}_{r,\mathrm{wl}}^{R_k} 2\pi)}{n_R}, \frac{\sum_{k=1}^{n_R} \sin(\hat{N}_{r,\mathrm{wl}}^{R_k} 2\pi)}{n_R}\right)/2\pi \quad (31)$$

$$d_{r,\mathrm{wl}}^E = \mathrm{atan2}\left(\frac{\sum_{k=1}^{n_E} \cos(\hat{N}_{r,\mathrm{wl}}^{E_k} 2\pi)}{n_E}, \frac{\sum_{k=1}^{n_E} \sin(\hat{N}_{r,\mathrm{wl}}^{E_k} 2\pi)}{n_E}\right)/2\pi \quad (32)$$

where n_G, n_C, n_R and n_E are the numbers of the WL ambiguities at current epoch for GPS, BDS, GLONASS and Galileo, respectively.

The results calculated by Eq. 29–32 may be biased because the expression is a nonlinear operator. Therefore, we regarded these results as the initial values of receiver UPDs, then the fractions of WL ambiguities were adjusted to be near the initial estimates. We further average the fraction parts of all WL ambiguities and the average value can be applied to estimate the receiver UPDs directly. The variances of four systems are calculated as following:

$$\sigma_{d_{r,\mathrm{wl}}^G}^2 = \frac{1}{n_G - 1} \sum_{k=1}^{n_G} (\hat{N}_{r,w}^{G_k} - N_{r,\mathrm{wl}}^{G_k} - d_{r,\mathrm{wl}}^G)^2 \quad (33)$$

$$\sigma_{d_{r,\mathrm{wl}}^C}^2 = \frac{1}{n_C - 1} \sum_{k=1}^{n_C} (\hat{N}_{r,\mathrm{wl}}^{C_k} - N_{r,\mathrm{wl}}^{C_k} - d_{r,\mathrm{wl}}^C)^2 \quad (34)$$

$$\sigma^2_{d^R_{r,\mathrm{wl}}} = \frac{1}{n_R-1}\sum_{k=1}^{n_R}(\hat{N}^{R_k}_{r,\mathrm{wl}} - N^{R_k}_{r,\mathrm{wl}} - d^R_{r,\mathrm{wl}})^2 \qquad (35)$$

$$\sigma^2_{d^E_{r,\mathrm{wl}}} = \frac{1}{n_E-1}\sum_{k=1}^{n_E}(\hat{N}^{E_k}_{r,\mathrm{wl}} - N^{E_k}_{r,\mathrm{wl}} - d^E_{r,\mathrm{wl}})^2 \qquad (36)$$

The estimated receiver UPDs are used to further correct the WL ambiguities. Therefore, the integer WL ambiguities and their variances can be obtained with:

$$N^{G_k}_{r,\mathrm{wl}} = \hat{N}^{G_k}_{r,\mathrm{wl}} - d^G_{r,\mathrm{wl}}, \quad \sigma^2_{N^{G_k}_{r,\mathrm{wl}}} = \sigma^2_{\hat{N}^{G_k}_{r,\mathrm{wl}}} + \sigma^2_{d^G_{r,\mathrm{wl}}} \qquad (37)$$

$$N^{C_k}_{r,\mathrm{wl}} = \hat{N}^{C_k}_{r,\mathrm{wl}} - d^C_{r,\mathrm{wl}}, \quad \sigma^2_{N^{C_k}_{r,\mathrm{wl}}} = \sigma^2_{\hat{N}^{C_k}_{r,\mathrm{wl}}} + \sigma^2_{d^C_{r,\mathrm{wl}}} \qquad (38)$$

$$N^{R_k}_{r,\mathrm{wl}} = \hat{N}^{R_k}_{r,\mathrm{wl}} - d^R_{r,\mathrm{wl}}, \quad \sigma^2_{N^{R_k}_{r,\mathrm{wl}}} = \sigma^2_{\hat{N}^{R_k}_{r,\mathrm{wl}}} + \sigma^2_{d^R_{r,\mathrm{wl}}} \qquad (39)$$

$$N^{E_k}_{r,\mathrm{wl}} = \hat{N}^{E_k}_{r,\mathrm{wl}} - d^E_{r,\mathrm{wl}}, \quad \sigma^2_{N^{E_k}_{r,\mathrm{wl}}} = \sigma^2_{\hat{N}^{E_k}_{r,\mathrm{wl}}} + \sigma^2_{d^E_{r,\mathrm{wl}}} \qquad (40)$$

In fact, after the satellite and receiver UPD correction, the WL ambiguities are still not integers because of unmodeled biases and random errors. Then fixing decision can be made according to the decision function based on hypothesis test theory (Dong and Bock 1989).

4.2 NL ambiguity fixing

If the WL ambiguities were fixed successfully, the corresponding float NL ambiguity can be obtained according to Eq. 16. The float NL ambiguities were corrected by satellite NL UPDs firstly. However, the NL ambiguities are still not close to the integer because of the receiver UPDs. Additionally, a singularity exists in the integer least-squares adjustment because of the strong linear correlation between the NL ambiguities and receiver clock bias. In order to separate the receiver UPD and receiver clock from the NL ambiguities, the NL ambiguity with the highest elevation is selected as a reference for each system, respectively. Then these reference NL ambiguities are fixed to the nearest integer to separate the receiver UPD and receiver clock bias. The reference ambiguities can be expressed as virtual observations:

$$N^{G_0}_{r,\mathrm{wl}} = [\hat{N}^{G_0}_{r,\mathrm{wl}}], \ P_{\tilde{N}^{G_0}_{r,\mathrm{wl}}} \in \infty \qquad (41)$$

$$N^{C_0}_{r,\mathrm{wl}} = [\hat{N}^{C_0}_{r,\mathrm{wl}}], \ P_{\tilde{N}^{C_0}_{r,\mathrm{wl}}} \in \infty \qquad (42)$$

$$N^{R_0}_{r,\mathrm{wl}} = [\hat{N}^{R_0}_{r,\mathrm{wl}}], \ P_{\tilde{N}^{G_0}_{r,w}} \in \infty \qquad (43)$$

$$N^{E_0}_{r,\mathrm{wl}} = [\hat{N}^{E_0}_{r,\mathrm{wl}}], \ P_{\tilde{N}^{E_0}_{r,\mathrm{wl}}} \in \infty \qquad (44)$$

where $[\cdot]$ represents rounding to the nearest integer; $N^{G_0}_{r,\mathrm{wl}}$ $N^{C_0}_{r,\mathrm{wl}}$ $N^{R_0}_{r,\mathrm{wl}}$ $N^{E_0}_{r,\mathrm{wl}}$ denote reference ambiguities for GCRE systems, respectively; $P_{N^{G_0}_{r,\mathrm{wl}}}$ $P_{N^{C_0}_{r,\mathrm{wl}}}$ $P_{N^{R_0}_{r,\mathrm{wl}}}$ and $P_{N^{E_0}_{r,\mathrm{wl}}}$

are the weights of reference ambiguities, respectively; the weight of the reference ambiguity is set as infinity ∞ in order to add a strong constraint to the observation equations.

After the reference ambiguity has been fixed, the receiver NL UPD of GPS is assimilated into receiver clock bias while the difference of receiver NL UPD between GPS and other systems is assimilated into ISB. However, the reference ambiguity may be biased by ΔN_{nl} cycles because the low precision of the float ambiguity. If the reference ambiguity is biased, the fixed values for all NL ambiguities in this system will be shifted by a common value of $\lambda_{\mathrm{nl}}\Delta N^0_{r,\mathrm{nl}}$ and the ambiguity for other satellites k can be expressed as:

$$\lambda^G_{\mathrm{nl}}\bar{N}^{G_k}_{r,\mathrm{nl}} + \lambda^G_{\mathrm{nl}}\Delta N^{G_0}_{r,\mathrm{nl}} = \lambda^G_{\mathrm{nl}}(\bar{N}^{G_k}_{r,\mathrm{nl}} + \Delta N^{G_0}_{r,\mathrm{nl}}) \qquad (45)$$

$$\lambda^C_{\mathrm{nl}}\bar{N}^{C_k}_{r,\mathrm{nl}} + \lambda^C_{\mathrm{nl}}\Delta N^{C_0}_{r,\mathrm{nl}} = \lambda^C_{\mathrm{nl}}(\bar{N}^{C_k}_{r,\mathrm{nl}} + \Delta N^{C_0}_{r,\mathrm{nl}}) \qquad (46)$$

$$\lambda^{R_k}_{\mathrm{nl}}\bar{N}^{R_k}_{r,\mathrm{nl}} + \lambda^{R_0}_{\mathrm{nl}}\Delta N^{R_0}_{r,\mathrm{nl}} = \lambda^{R_k}_{\mathrm{nl}}(\bar{N}^{R_k}_{r,\mathrm{nl}} + \Delta N^{R_0}_{r,\mathrm{nl}})$$
$$+ \Delta N^{R_0}_{r,\mathrm{nl}}(\lambda^{R_0}_{\mathrm{nl}} - \lambda^{R_k}_{\mathrm{nl}}) \qquad (47)$$

$$\lambda^E_{\mathrm{nl}}\bar{N}^{E_k}_{r,\mathrm{nl}} + \lambda^E_{\mathrm{nl}}N^{E_0}_{r,\mathrm{nl}} = \lambda^E_{\mathrm{nl}}(\bar{N}^{E_k}_{r,\mathrm{nl}} + N^{E_0}_{r,\mathrm{nl}}) \qquad (48)$$

where $\bar{N}^{G_k}_{r,\mathrm{nl}}$, $\bar{N}^{C_k}_{r,\mathrm{nl}}$, $\bar{N}^{R_k}_{r,\mathrm{nl}}$ and $\bar{N}^{E_k}_{r,\mathrm{nl}}$ are float ambiguities of satellite G_k, C_k, R_k and E_k. For GPS, BDS and Galileo, the bias in the reference ambiguity will cause an integer offset for other ambiguities, which will not affect the ambiguity resolution. For GLONASS, it is noted that the second term of Eq. 47, namely $\Delta N^{R_0}_{r,\mathrm{nl}}(\lambda^{R_0}_{\mathrm{nl}} - \lambda^{R_k}_{\mathrm{nl}})$, destroy the integer nature of the final ambiguity of satellite. Since the maximum difference in the NL wavelength between two GLONASS satellites is less than 0.0005 m, if the float ambiguity has the precision of 1 m, the extra bias $\Delta N^{R_0}_{r,\mathrm{nl}}(\lambda^{R_0}_{\mathrm{nl}} - \lambda^{R_k}_{\mathrm{nl}})$ will be less than 0.005 m and such a small bias will not affect the ambiguity fixing for other ambiguities.

We performed the dual-frequency multi-GNSS PPP AR based on the observation data on L1 and L2 frequencies for GPS and GLONASS, B1 and B2 frequencies for BDS and E1 and E5a frequencies for Galileo. An elevation-dependent weighting strategy was applied for ambiguity-fixed PPP to mitigate the effects of multipath as well as atmospheric errors. The precision for phase raw observables and code raw observables for both GPS and GLONASS system is 3 mm and 0.3 m, while 6 mm and 0.6 m for BDS and Galileo system. The satellite-induced code bias correction is also applied to obtain the high-precision PPP float ambiguities for BDS. The precision of satellite orbit will also influence the NL ambiguity resolution especially for BDS GEO satellites, which cannot be fixed correctly sometimes because of the poor precision of orbit. In a small region, the elevation angle for a GEO satellite will be almost the same for each station, which will cause a similar orbit error for each station. Then the orbit errors are absorbed by the NL UPDs estimated by these regional stations. The IFBs for GLONASS NL ambi-

guities can be ignored for users since the IFBs are absorbed by the NL UPDs.

## 5 The UPD results for GPS, BDS, GLONASS and Galileo

5.1 GPS UPDs

The observations of 148 stations all over the world from the IGS and MGEX network are used for GPS UPD estimation here. The distribution of the selected stations for UPD estimation is shown in Fig. 3. It is clear that there are three main regions in which dense station-nets can be found, and these regions are North America, Europe and a region extending from Australia to the East Asia. The time span of the GPS UPD estimation is 30 days, from day of year (DOY) 001 to

030 in 2017. In general, 140 stations are used for UPD estimation except a few stations failed in downloading observation files from CDDIS FTP server or that be excluded from processing because of frequent data interruption.

The time series of daily estimated GPS WL UPDs are shown in Fig. 4. The satellite G04 is usually at abnormal status and therefore G04 is removed from our estimation. Note that we adjusted the WL UPDs by adding ± 1 cycle in order to keep the consistence of WL UPD time series shown in Fig. 4. The G03 presents the largest variation, which is about 0.125 cycles between the minimum and maximum UPD values. The mean STD of all satellites is 0.023 cycles, in which the largest STD is 0.034 cycles for G03. From Fig. 4, we can conclude that the GPS WL UPDs are rather stable even for one month.

For NL UPD processing, multi-GNSS precise orbit and clock from GFZ are used for four-system float PPP and the

Fig. 3 Distribution of the GNSS ground network, which was used for the GPS UPD estimation. North America, Europe and a region extending from Australia to the East Asia are the three most dense regions
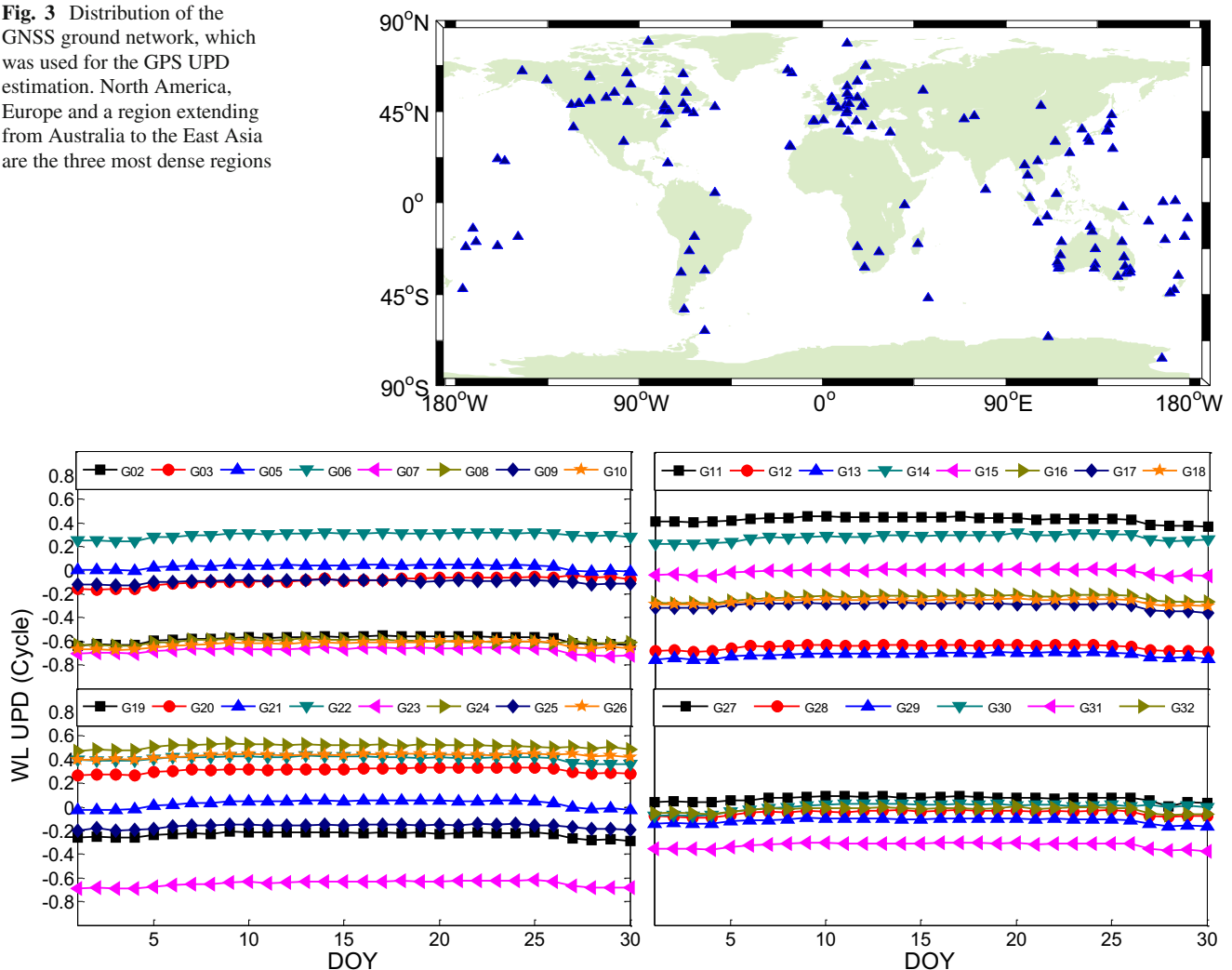
Fig. 4 Estimated GPS WL UPDs. The time span is 30 days, from DOY 001 to 030 in 2017, and G01 is taken as the reference at each day. Different colors represent different satellites
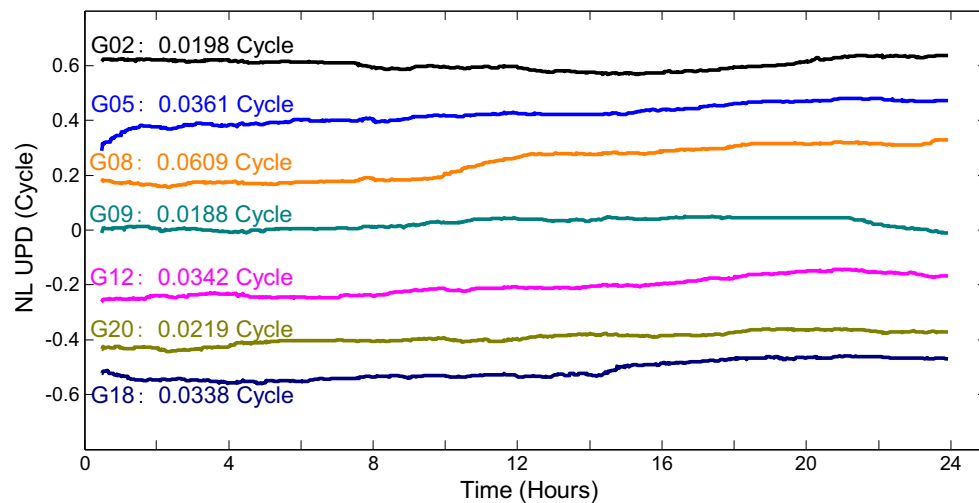
Fig. 5 GPS NL UPDs in DOY 001 of 2017 for seven exemplary satellites estimated every epoch (30 s). Different colors represent different satellites
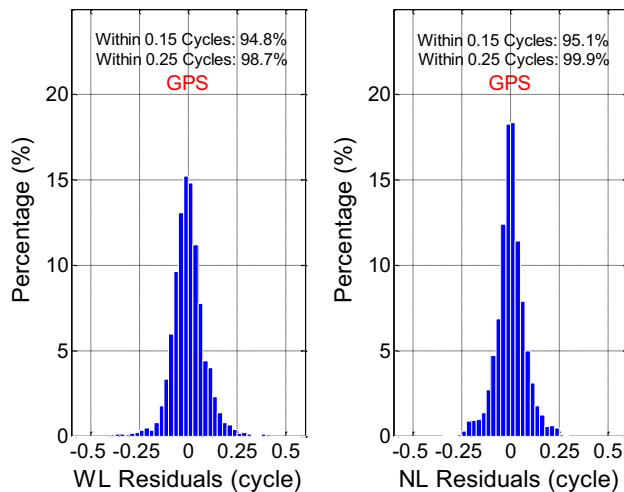
Fig. 6 Residual distributions of the GPS WL (left panel) fractional parts (in cycles) and NL (right panel) fractional parts (in cycles) after removal of UPDs

UPD are estimated epoch by epoch based on all float ambiguities. Our results show that, all GPS satellites have stable NL UPDs with a daily change of smaller than 0.2 cycles and the mean STD of NL UPD of 30 days is 0.04 cycles, and the difference between two adjacent epochs is smaller than 0.05 cycles. We present the NL UPDs results of some exemplary satellites in Fig. 5, and the largest STD is found at satellite G08 with the STD of 0.061 cycles.

After the separation of both WL and NL UPDs, the ambiguities should be close to integers. The residuals can be expressed by the difference between the float ambiguities after removal of UPDs and the nearest integers, in other words, the fractional parts of the float ambiguities after removal of estimated UPDs. The histograms of both WL residuals and NL residuals are shown in Fig. 6. For WL ambi-

guities, 94.8% of the residuals are within ±0.15 cycles, while 98.7% residuals are within ±0.25 cycles; as for NL ambiguities, the percentages of residuals within ±0.15 cycles and ±0.25 cycles are 95.1 and 99.9%, respectively. The average values of WL and NL residuals are both 0, and the RMS are 0.086 (for WL) and 0.076 (for NL) cycles, which indicates that the NL residuals have a slightly better distribution more concentrated around the zero than that of WL.

5.2 BDS UPDs

5.2.1 MGEX global network

About 67 stations from the MGEX network, Fig. 2, are used for BDS UPD estimation. To evaluate the influence of BDS code bias on BDS UPDs, we perform the UPD estimation on observations before and after the code bias correction, respectively. Data of 30 days from DOY 001 to DOY 030 of 2017 is processed. The mean STDs of WL and NL UPDs of 30 days before and after the code bias correction were also calculated and are shown in Table 3. Figure 7 demonstrates the WL UPDs of BDS satellites before (*upper* panels) and after (*bottom* panels) the code bias correction, with respect to C06. Different satellite block types are shown in different panels. For GEO satellites, the WL UPDs before the code bias correction have a mean STD of 0.154 cycles, while the mean STD is 0.111 cycles after the code bias correction, with an improvement of 27.9%. For WL UPDs of IGSO satellites, an improvement of 77.9% in mean STD is made by the code bias correction, from 0.093 to 0.021 cycles. As for MEO satellites, the improvement is 88.9% from 0.229 to 0.025 cycles. It is then concluded that after the code bias correction, WL UPDs of all three constellations are more stable and reliable. The WL UPDs of the IGSO and MEO satellites are more stable

Table 3 Mean STDs of WL and NL UPDs for MGEX global network before and after the code bias correction (Unit: cycles)

	WL UPD		NL UPD	
	uncorrected	corrected	uncorrected	corrected
GEO	0.154	0.111	0.046	0.044
IGSO	0.093	0.021	0.036	0.028
MEO	0.229	0.025	0.062	0.048

than the GEO satellites since the GEO satellites suffer severe multipath error and cannot be completely eliminated by the wavelet transform correction. We notice that after the code bias correction, for C14, a jump of 0.44 cycles between DOY 021 and 022 and a jump of 0.23 cycles between DOY 025 and 026 are happened. The frequent jumps were found for WL UPDs of some BDS satellites and then we also found that the precise clock corrections of these satellites provided by Wuhan University and GFZ experienced datum offsets on those days. However, the reason for the offset of BDS WL UPD was not clear and needed further investigation (Li et al. 2016). The similar phenomenon is also found in C13 between DOY 019 and 020, C03 between DOY 009 and 010, and C03 between DOY 022 and 023 after the code bias correction. The frequent jumps caused by clock datum offset will not affect the PPP AR when the same clock file is used for UPD estimation and PPP AR.

In Fig. 8, NL UPDs at DOY 001 of 2017 are illustrated. The mean STDs of NL UPDs from DOY 001 to DOY 030 of

2017 were also shown in Table 3. The improvements caused by removing the code biases are 4.3, 22.2 and 22.5% for GEO, IGSO, and MEO satellites, respectively. Since the WL ambiguities are already fixed, the quality of the estimated NL UPDs are dominated by the precision of the IF ambiguities. In fact, IF ambiguities are affected by the code biases slightly because code observations are assigned a much lower weight than the carrier phase observations. It is reasonable that the improvements of the NL UPDs after the code bias correction are not as significant as the WL results.

The distributions of WL and NL residuals before and after the code bias correction are demonstrated in Fig. 9 and Table 7 in Appendix. For WL residuals, it is clear that the residuals of MEO satellites have significant improvement after removing code biases while no obvious improvements are found for GEO and IGSO satellites. For NL UPDs, the residual distribution of BDS satellites after the code bias correction is slightly better than uncorrected one. The percentages of GEO NL residuals within ± 0.15 cycles are evidently smaller than that of IGSO and MEO satellites because of the worse orbit quality of GEO satellites. Meanwhile, the percentages of NL residuals within ± 0.25 cycles are close to 100% for all GEO, IGSO, and MEO satellites after the code bias correction.

### 5.2.2 Regional networks

BDS UPDs are also estimated by the two regional networks shown in Fig. 2. The estimated WL and NL UPDs for
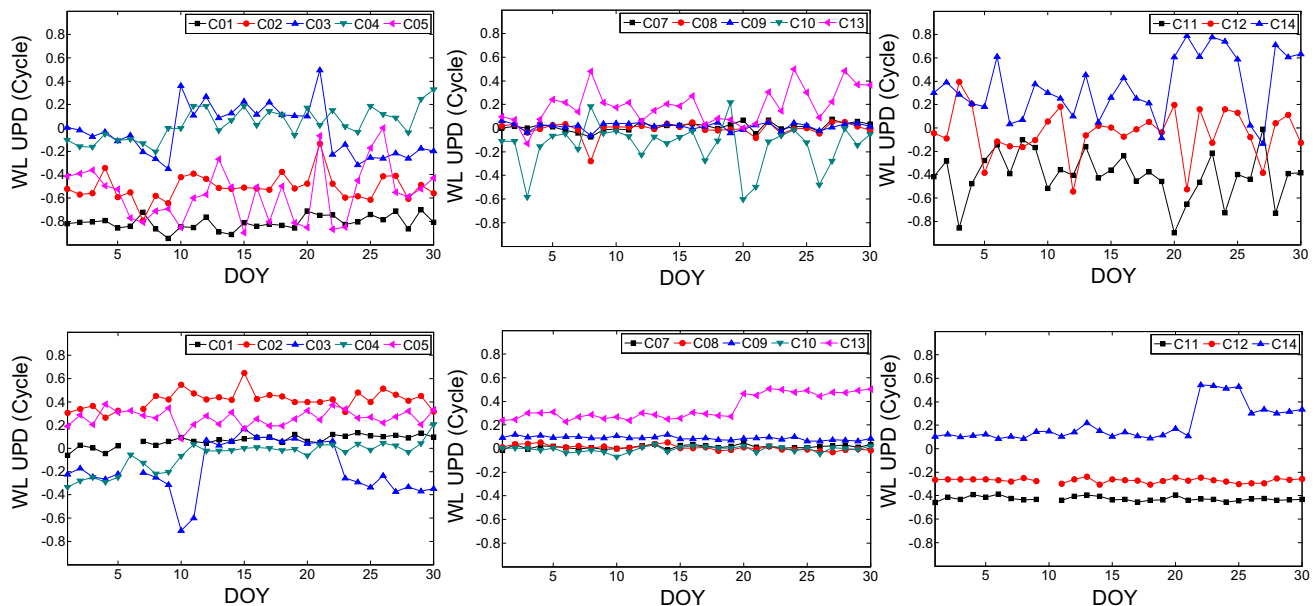

Fig. 7 BDS WL UPDs of 30 days from DOY 001 to DOY 030 of 2017, using MGEX observations. The upper panels represent BDS WL UPDs before the code bias correction, while the bottom panels represent that after the code bias correction. Different satellite block types are shown in different panels, from left to right: GEO, IGSO and MEO
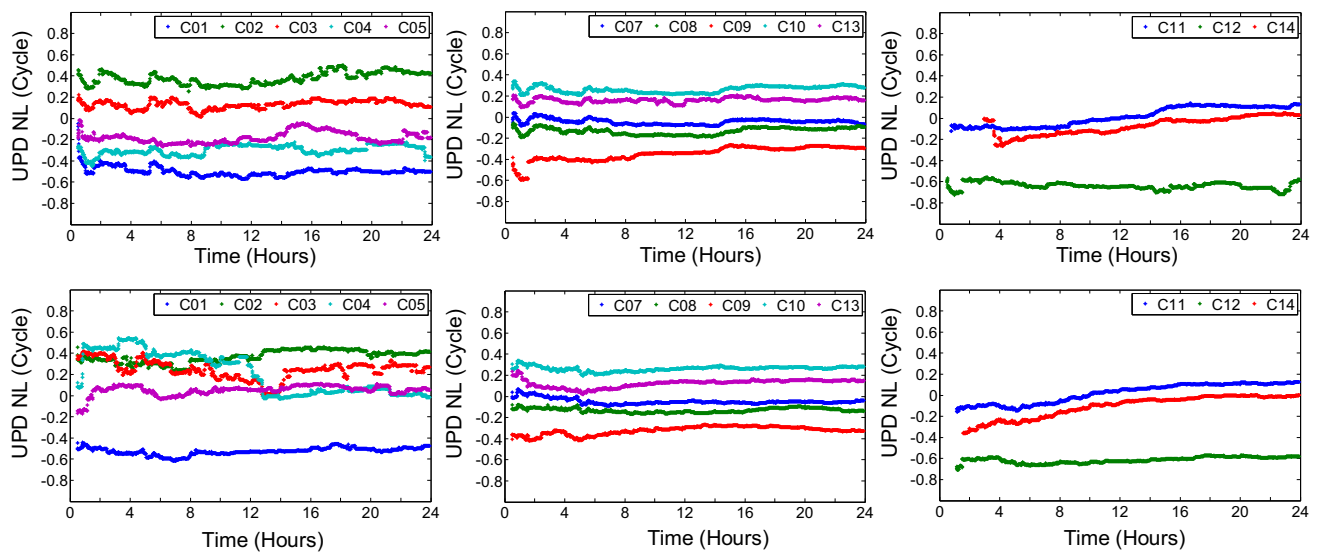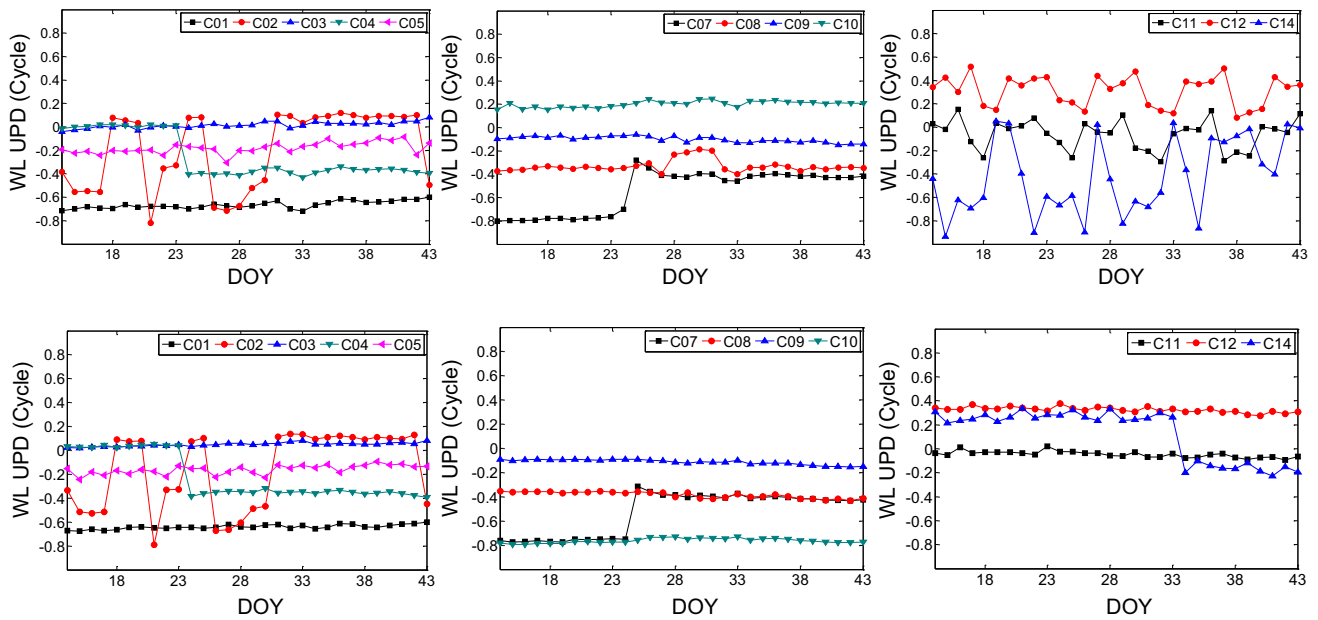
Fig. 8 BDS NL UPDs of DOY 001 of 2017 before (upper panels) and after (bottom panels) the code bias correction. Different satellite block types are shown in different panels, from left to right: GEO, IGSO and MEO
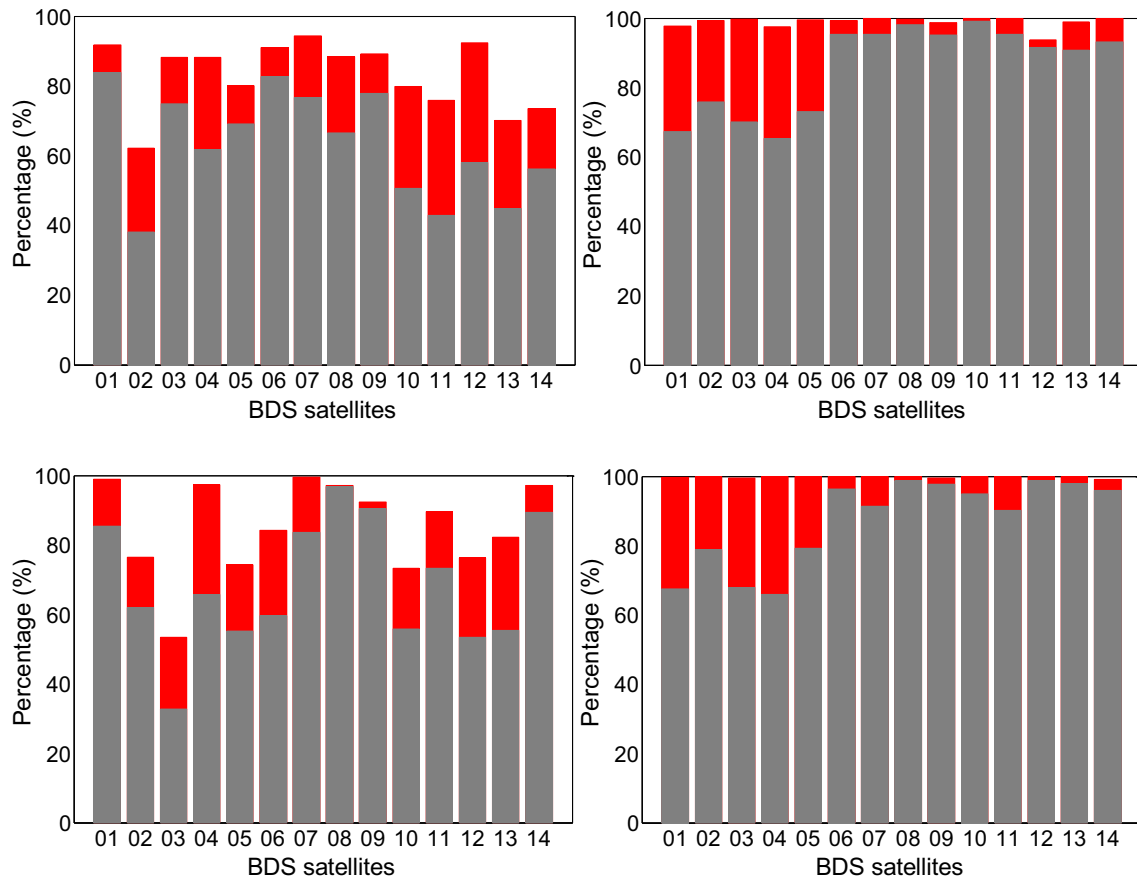
Fig. 9 Distributions of BDS WL (left) and NL (right) residuals before (upper) and after (bottom) the code bias correction. The gray bars represent percentages of residuals within ±0.15 cycles while the red bars represent percentages of residuals with ±0.25 cycles
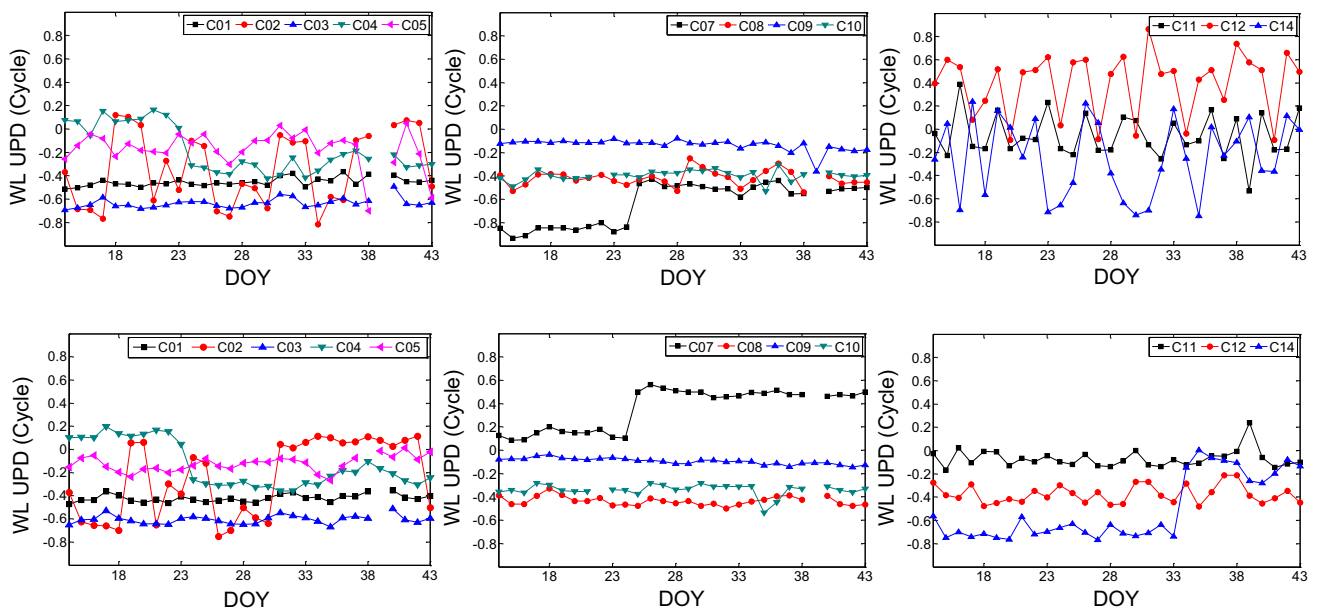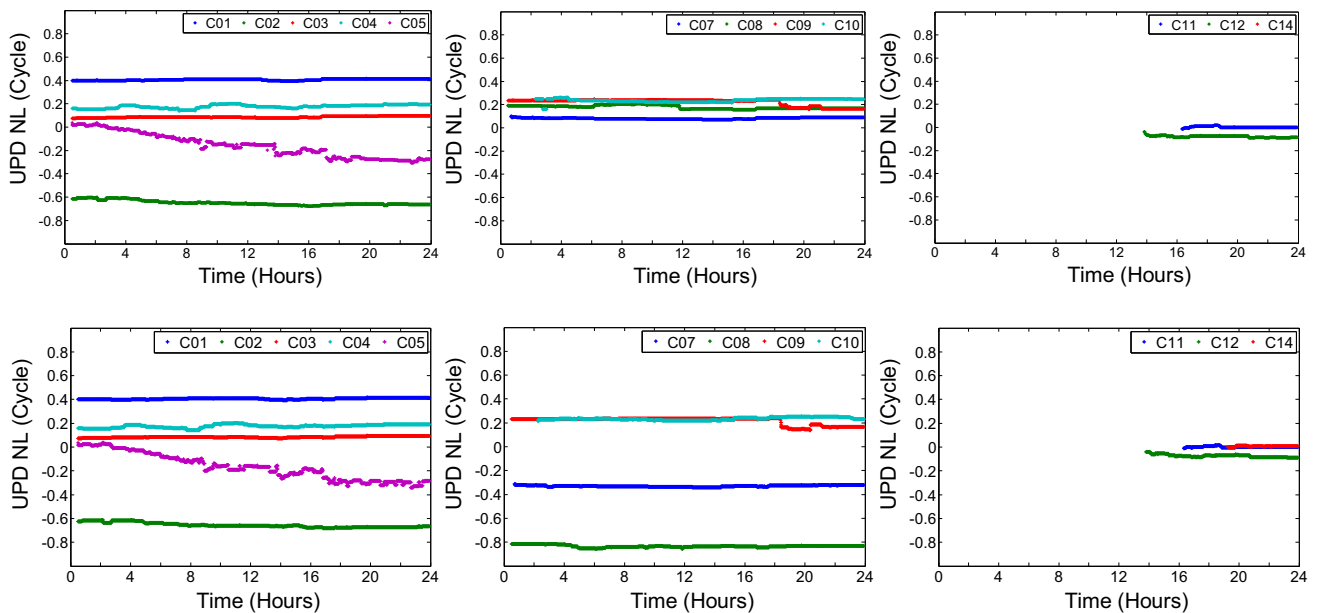
Fig. 10 BDS WL UPDs from the CMONOC. The upper and bottom panels are for WL UPDs before and after the code bias correction, respectively. Different satellite block types are shown in different panels, from left to right: GEO, IGSO and MEO
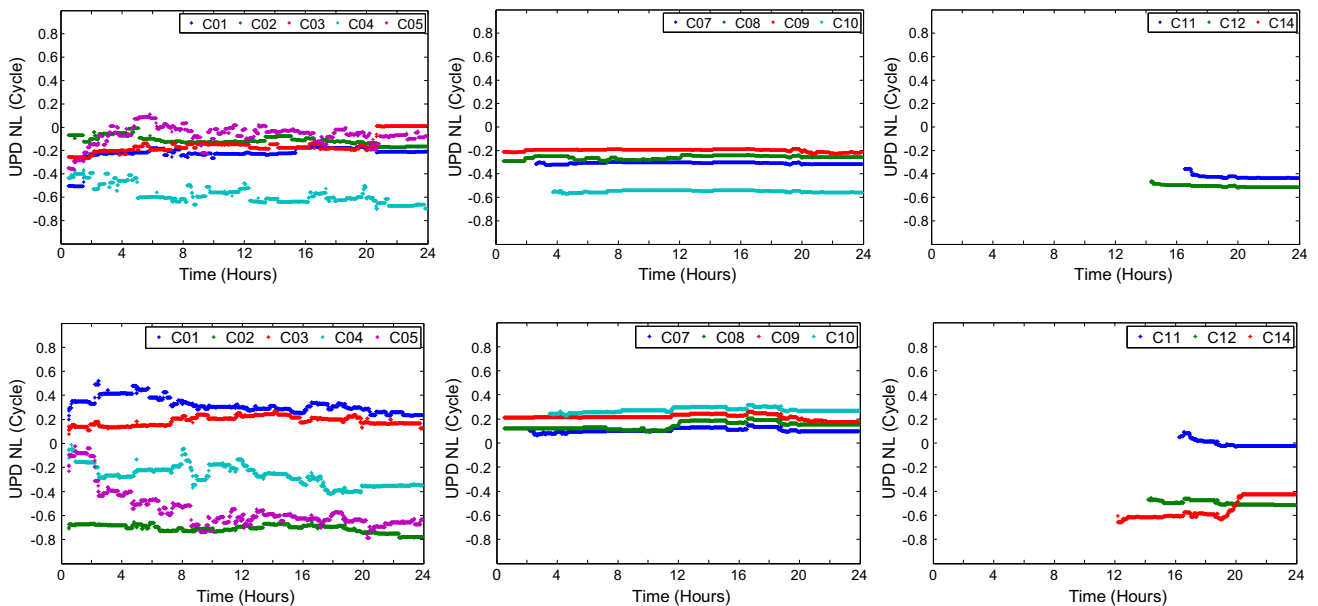
Fig. 11 BDS NL UPDs from CMONOC. The upper and bottom panels are for NL UPDs before and after the code bias correction, respectively. Different orbit types are shown in different subplots

CMONOC and Hong Kong CORS are shown in Figs. 10, 11, 12, 13 and the mean STD of WL and NL UPDs of days from DOY 001 to DOY 030 of 2016 are given in Tables 4, 5. Results show that WL UPDs from CMONOC have better stabilities when the code biases are corrected with the improvements of 16.7, 27.6 and 85.9% for GEO, IGSO and MEO satellites, respectively. The frequent jump was found for C02 satellite. We also found that the precise clock corrections of C02 provided by Wuhan University and GFZ experienced frequent

clock datum offsets between DOY 001 and 030. The jump at C04 between DOY 023 and 024, the jump at C07 between DOY 024 and 025, and the jump at C14 between DOY 033 and 034, are also caused by the same reason. For Hong Kong CORS WL UPDs, the improvements of mean STD are 11.7, 12.1 and 74.4% for GEO, IGSO, and MEO satellites after the code bias correction. The improvements of UPDs for MEO satellites are more significant than IGSO and GEO UPDs because the MEO satellites suffer severe code bias. Among

Fig. 12 BDS WL UPDs from Hong Kong CORS network. The upper and bottom panels are for WL UPDs before and after the code bias correction, respectively. Different satellite block types are shown in different panels, from left to right: GEO, IGSO and MEO

Fig. 13 BDS NL UPDs from Hong Kong CORS network. The upper and bottom panels are for NL UPDs before and after the code bias correction, respectively. Different satellite block types are shown in different panels, from left to right: GEO, IGSO and MEO

the three types of BDS satellites, the GEO and IGSO satellites are visible for longer periods than MEO satellites in East-Asia area, which is helpful to smooth out code biases of GEO and IGSO satellites. The GEO WL UPDs of regional network are much more stable compared to results of global network before the code bias correction since the code bias are similar for each station in a small network and then will be assimilated to the satellite UPDs.

Table 4 Mean STDs of WL and NL UPDs for CMONOC before and after the code bias correction (Unit: cycles)

	WL UPD		NL UPD	
	uncorrected	corrected	uncorrected	corrected
GEO	0.030	0.025	0.072	0.074
IGSO	0.029	0.021	0.013	0.020
MEO	0.198	0.028	0.017	0.023

Table 5 Mean STDs of WL and NL UPDs for Hong Kong CORS network before and after the code bias correction (Unit: cycles)

	WL UPD		NL UPD	
	uncorrected	corrected	uncorrected	corrected
GEO	0.060	0.053	0.031	0.029
IGSO	0.066	0.058	0.015	0.013
MEO	0.266	0.068	0.008	0.007

As for NL UPDs, the mean STDs for CMONOC of 30 days are 0.072, 0.013 and 0.017 cycles (before the code bias correction), and 0.074, 0.020 and 0.023 cycles (after the code bias correction) for GEO, IGSO and MEO, respectively. For Hong Kong CORS (in Fig. 13), the mean STDs of NL UPDs are 0.031, 0.015, and 0.008 cycles (before the code bias correction), and 0.029, 0.013, and 0.007 cycles (after the code bias correction) for GEO, IGSO and MEO. Whether code biases are corrected or not, BDS NL UPDs are rather stable for both CMONOC and Hong Kong CORS networks. The NL UPD of C14 is not available before the bias correction since ambiguity observations with a large residual are removed during the process of the NL UPD estimation. After the code bias correction, the NL UPDs of C14 satellite is available for both CMONOC and Hong Kong network. Hong Kong CORS network has NL UPDs of the smallest mean STD, and it is attributed to the higher correlation of orbit errors among stations as a result of denser distribution.

5.3 GLONASS UPDs

For GLONASS, the method of a UPD estimation using homogeneous receivers was applied. We performed here the GLONASS UPD estimation for three different receivers, namely TRIMBLE NETR9 receivers, LEICA receivers and JAVAD TRE_G3TH DELTA receivers. It has been observed that GLONASS code IFBs vary with not only receiver types, but also firmware, domes and antennas (Geng and Bock 2016). To analyze the effect of firmware type on the estimation of GLONASS UPD, the receivers with the same and mixed firmware version were both used to estimate UPD. For TRIMBLE NETR9, there are 92 stations out of MGEX and traditional IGS network all over the world. If we take the hardware version into consideration, the version 5.15 of TRIMBLE NETR9 has the most stations of 48. As for receivers made by LEICA, there are many different types and versions, so all 57 stations with LEICA receivers will be put together to estimate UPDs. For JAVAD TRE_G3TH DELTA receivers, version 3.6.7 is chosen and only 17 stations are found in MGEX and IGS network. The distributions of stations are shown in Fig. 14, with the different colors and shapes representing different receiver types or versions.

Four panels in Fig. 15 show the estimated GLONASS WL UPDs with respect to R01, and panels from (a) to (d) represents the WL UPDs from all TRIMBLE NETR9 receivers, TRIMBLE NETR9 5.15 receivers, all LEICA receivers and JAVAD TRE_G3TH DELTA version 3.6.7 receivers, respectively. Note that there are no values for satellite R23 at DOY 008 in all four panels. According to the GLONASS information and analysis center website (http://www.glonass-center. ru/en/archive/), only 23 satellites were in operational status and R23 was in maintenance status. At the same time, satellite R21 has large jumps on DOY 015 for all the four WL UPD results, and the jump values are 0.34, 0.33, 0.25 and 0.42 cycles for (a), (b), (c) and (d), respectively. Again, 'changes in spacecrafts' were reported on the GLONASS Website at DOY 014. We believe this jump is caused by the changes in the spacecraft status, like other researchers illustrated (Liu et al. 2017b).

The mean STDs of WL UPDs shown in Table 6 are 0.039 cycles for TRIMBLE NETR9 all versions receivers, 0.045 cycles for TRIMBLE NETR9 5.15 receivers, 0.049 cycles for LEICA receivers, and 0.056 cycles for JAVAD TRE_G3TH DELTA 3.6.7 receivers. The number of stations using TRIMBLE NETR9 all versions receivers is nearly two times as many as that of stations using TRIMBLE NETR9 version 5.15 receivers, and thus the former WL UPDs are more stable than the latter. The results of LEICA receivers are also stable in spite of different receiver types and versions. The worst behavior can be found in WL UPDs estimated by JAVAD TRE_G3TH DELTA 3.6.7 receivers. Results demonstrate that the WL UPD values of inhomogeneous receivers are different with others, however, different firmware versions seem to have no effect of the WL UPDs for the same type of receiver such as TRIMBLE NETR9 and LEICA receivers.

The NL UPD results are given in Fig. 16 and the mean STDs of NL UPDs of 30 days estimated by different types of receivers are shown in Table 6. The mean STDs of NL UPDs estimated by TRIMBLE NETR9 all version receivers, TRIMBLE NETR9 5.15 receivers, LEICA receivers and JAVAD TRE_G3TH DELTA 3.6.7 receivers are 0.092, 0.095, 0.108 and 0.099 cycles, respectively. The NL UPDs estimated by LEICA receivers show the worst stability, while the other three have very close mean STDs of about 0.095 cycles. The GLONASS UPDs cannot be estimated correctly by mixed types of receivers since the UPD values of different types of receivers are also different. However, the stable UPDs can be estimated by TRIMBLE NETR9 or LEICA receivers with mixed firmware, which demonstrated that different firmware versions have no obvious influence on the UPD estimation for TRIMBLE NETR9 and LEICA receivers. Experiments in Sect. 6 also indicate that UPDs estimated by receivers with mixed firmware can be used for successful ambiguity resolution. Although the NL UPDs are not as stable as the

Fig. 14 Distribution of GLONASS networks for UPD estimation. The black dots denote the stations with receiver JAVAD TRE_G3TH DELTA (version 3.6.7); the green squares denote the stations with LEICA receivers, taking no account of specific type or version; the blue triangles denote the stations with receiver TRIMBLE NETR9, regardless of version; while the red triangles denote the stations with receiver TRIMBLE NETR9 (version 5.15)
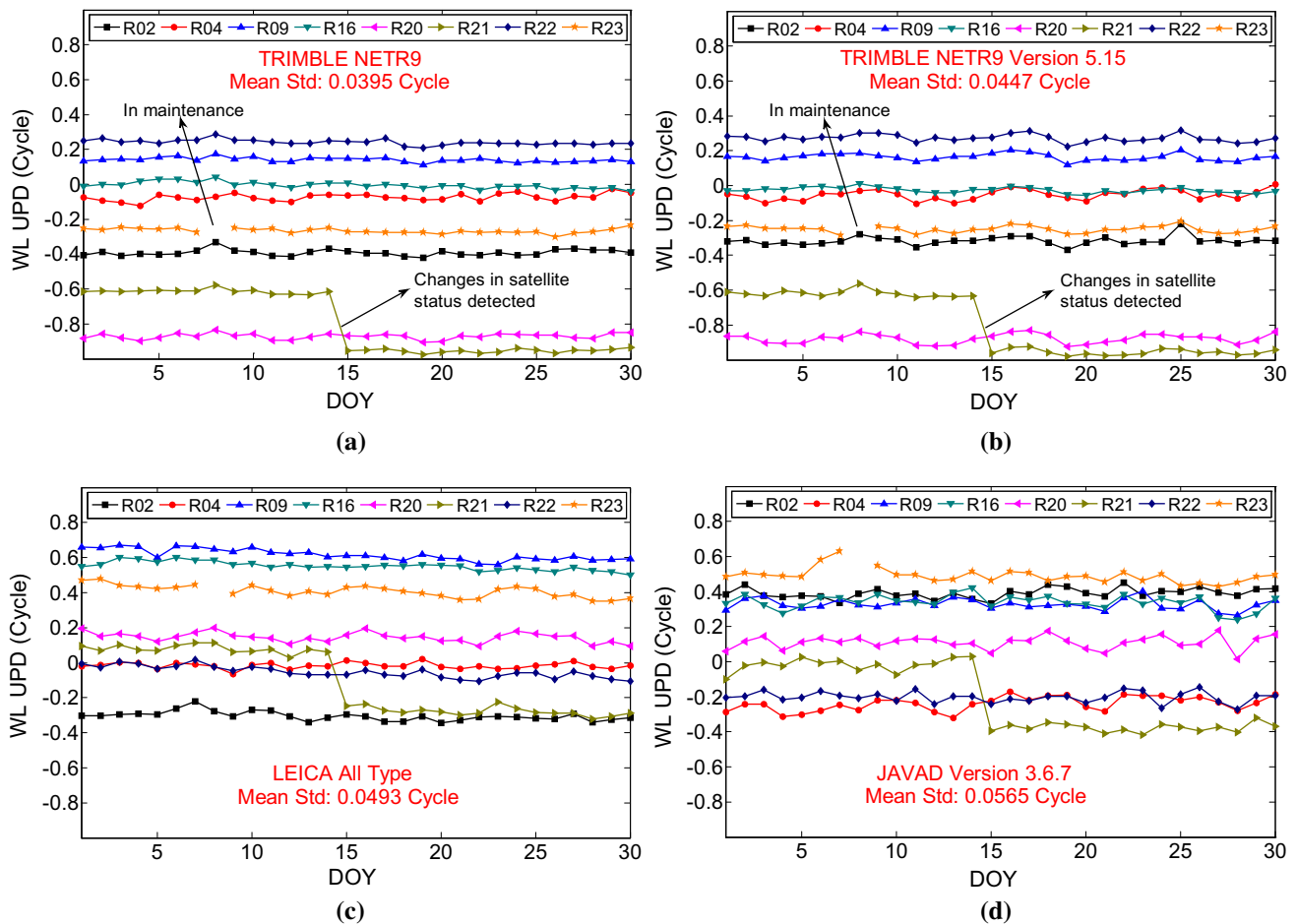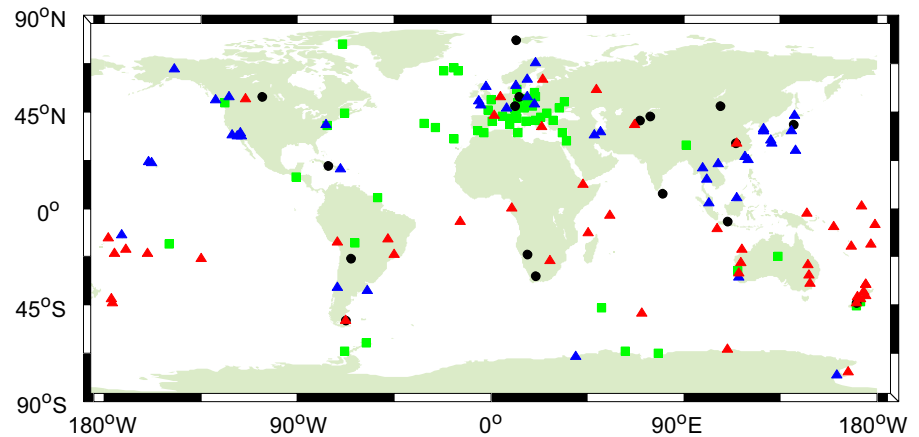

Fig. 15 GLONASS WL UPDs, with R01 being the reference satellite. Each subplot from **a** to **d** represents WL UPDs estimated from TRIMBLE NETR9 all version receivers, TRIMBLE NETR9 5.15 version receivers, LEICA receivers, and JAVAD TRE_G3TH DELTA version 3.6.7 receivers, respectively

Table 6 Mean STDs of WL and NL UPDs estimated from different types of receivers. (unit: cycles)

	TRIMBLE NETR9 all version	TRIMBLE NETR9 5.15	LEICA	JAVAD TRE_G3TH DELTA
WL UPD	0.039	0.045	0.049	0.056
NL UPD	0.092	0.095	0.108	0.099
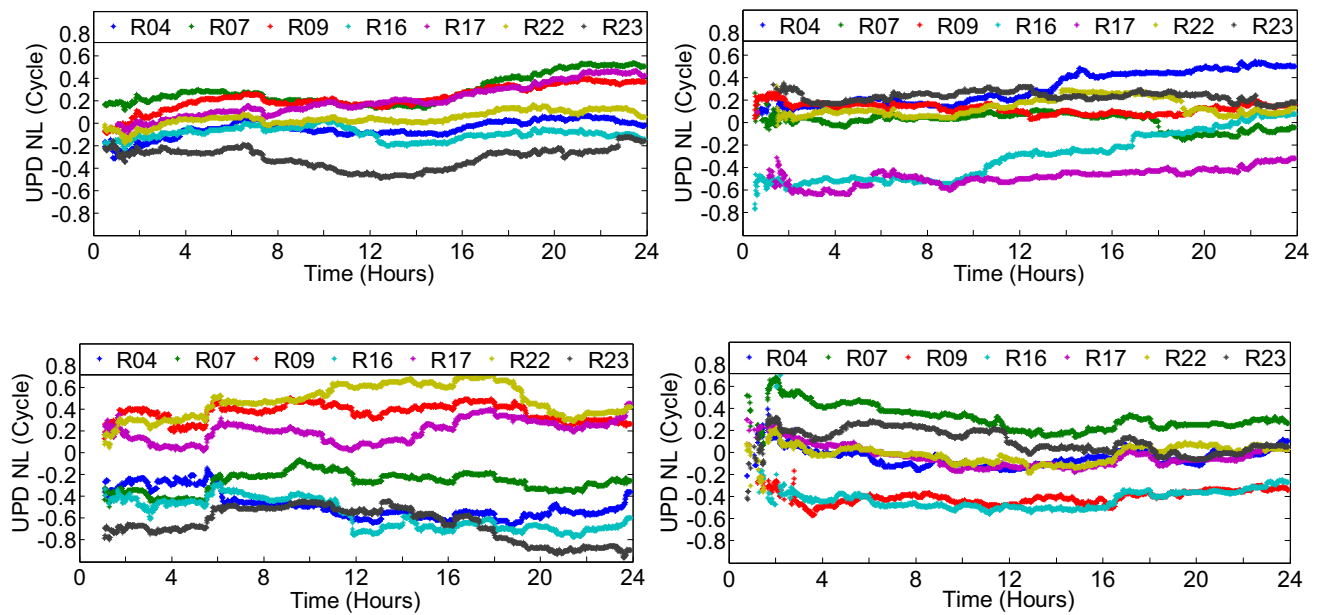
Fig. 16 NL UPDs of GLONASS satellites. The left-upper is for TRIMBLE NETR9 all version receivers, with the right-upper for TRIMBLE NETR9 5.15 receivers, the left-bottom for LEICA receivers and the right-bottom for JAVAD TRE_G3TH DELTA 3.6.7 receivers
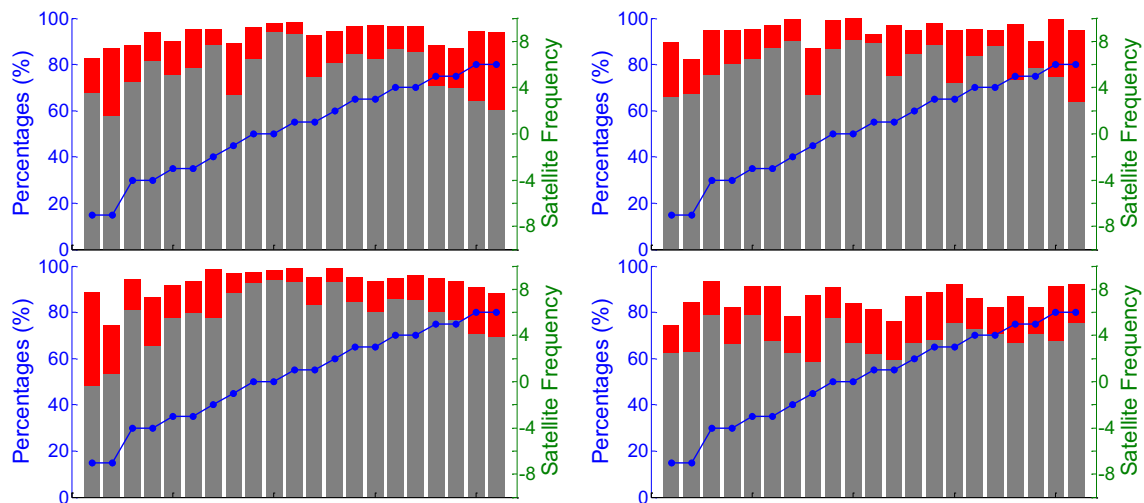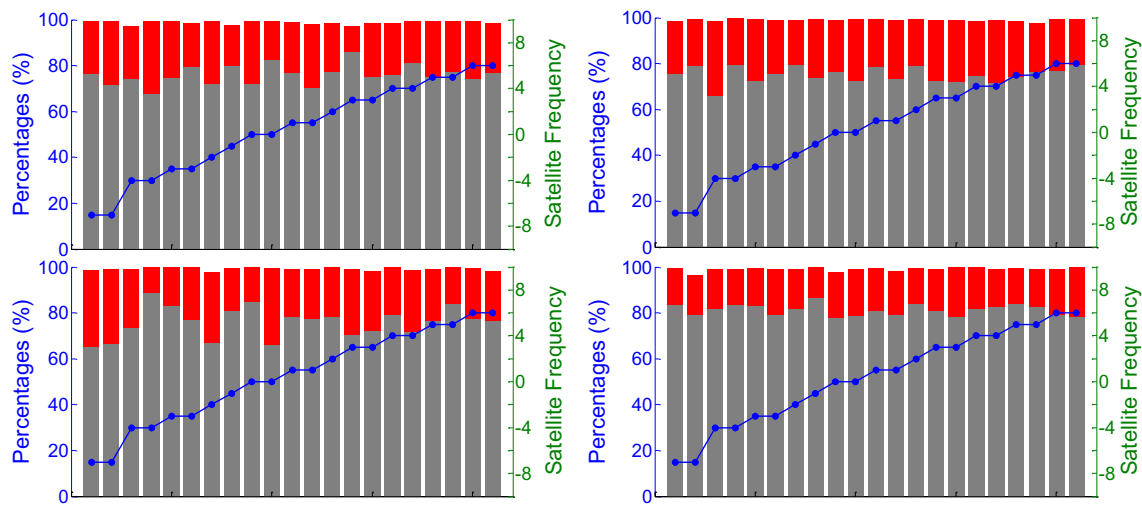

Fig. 17 Percentage distribution of the fractional parts of WL ambiguities after applying the WL UPDs within ±0.25 (red) and ±0.15 (gray), and satellite frequency (blue). The left-upper subplot denotes the result of TRIMBLE NETR9 all version receivers; the right-upper subplot denotes the result of TRIMBLE NETR9 V. 5.15 receivers; the bottom-left subplot denotes the result of LEICA all type all version receivers; the bottom-right one denotes that of JAVAD TRE_G3TH DELTA V. 3.6.7 receivers

GPS UPDs which have a mean STD of 0.04 cycles, the NL UPDs which have a mean STD less than 0.11 cycles are stable enough to fix the NL ambiguities.

Figures 17 and 18 demonstrate the distribution of WL and NL residuals, after correcting float ambiguities with estimated UPDs and the statistical results also shown in Table 8 in Appendix. In Fig. 17, it is clear that JAVAD TRE_G3TH DELTA 3.6.7 receivers have the lowest percentages of WL residuals within both ±0.15 and ±0.25 cycles, while TRIM-

BLE NETR9 5.15 receivers have the highest percentages. However, even WL residuals of TRIMBLE NETR9 5.15 receivers, which show the best performance among four different receivers, are relatively poor when compared with GPS WL residuals: 94.8% within ±0.15 cycles and 98.7% within ±0.25 cycles. In Fig. 18, the NL UPDs estimated by JAVAD TRE_G3TH DELTA 3.6.7 receivers have the highest percentage of residuals within ±0.15 cycles, while the rest three have similar values of about 75%. The percentages of NL

Fig. 18 Percentage distribution of the fractional parts of all NL ambiguities with fixed WL ambiguities after applying the NL UPDs within ± 0.25 (red) and ± 0.15(gray), and satellite frequency (blue). The four subplots share the same order with Fig. 17

residuals within ± 0.25 cycles are all close to 100% in four situations.

5.4 Galileo UPDs

Stations of European and global networks were used to generate the Galileo UPDs and two types of UPD products were analyzed and evaluated. The European network consists of 37 MGEX stations and 12 IGS stations with Galileo observations, and the global network consists of 142 MGEX stations and 53 IGS stations including 49 stations in Europe, as shown in Fig. 19. The WL UPDs from DOY 001 to DOY 030 of 2017 are shown in Fig. 20. The mean STDs of global and European WL UPDs are 0.01 cycles and 0.02 cycles, respectively, which indicates that the global WL UPDs are slightly more stable than European WL UPDs. However, when compared with WL UPDs of GPS, BDS and GLONASS, both global and European Galileo WL UPDs show best performance in term of mean STD. It means that although the Galileo constellation is still undergoing, the WL UPDs of Galileo can be determined with the best accuracy among four global navigation systems.

Figure 21 shows the NL UPDs at 6 exemplary satellites, i.e., E18, E19, E22, E24, E26 and E30. We notice that the NL UPDs from either global stations or European stations share a similar stability. The mean STD of NL UPDs of 30 days estimated from global network is 0.089 cycles, while the mean STD of NL UPDs from European network is 0.105 cycles. These mean STDs are comparable to those of GLONASS NL UPDs, while bigger than that of GPS and BDS. It can be concluded that although there are only 13 available Galileo satellites, the NL UPDs can still be estimated with reliable accuracy.

In Fig. 22 the distributions of WL and NL residuals are demonstrated. The percentages of WL residuals within ± 0.15 cycles and ± 0.25 cycles are 96.5 and 99.1% (for European network) comparing with 92.0 and 97.7% (for global network), and the percentages of NL residuals within above thresholds are 93.8 and 99.8% (for European network) and 86.7 and 99.0% for European network. The average residuals are all close to zero, and the RMS of WL and NL residuals are 0.091 and 0.107 cycles for global network, 0.072 and 0.082 cycles for European network, respectively. It is noticeable that, for both WL and NL residuals, the European ones are more concentrated around the zero than global ones. One possible reason for this phenomenon is that the European network has a denser distribution than the global network, so each station in European network will suffer from similar errors. The similar errors will be absorbed by the satellite UPDs, which will result in a better residual distribution.

6 Result analysis of multi-GNSS PPP AR

The PPP AR performance in terms of TTFF, positioning accuracy and fixing percentage of single-, dual-, and four-system PPP solutions are compared and analyzed. The convergence time and positioning accuracy of PPP float solutions are also analyzed for comparison. For the purpose of this study, convergence time is defined as the time required to achieve a horizontal accuracy less than 5 cm and the TTFF was defined as the time taken for the first ambiguity to be successfully fixed (Feng and Wang 2008; Gao et al. 2015). The positioning accuracy was assessed by comparing PPP coordinates with reference coordinates from the network solution with PANDA software (Liu and Ge 2003). Additionally, the

Fig. 19 Distribution of stations used in GALILEO UPD estimation. The red triangles represent stations in Europe, with the blue triangles in other areas, and together both blue and red triangles represent the global network
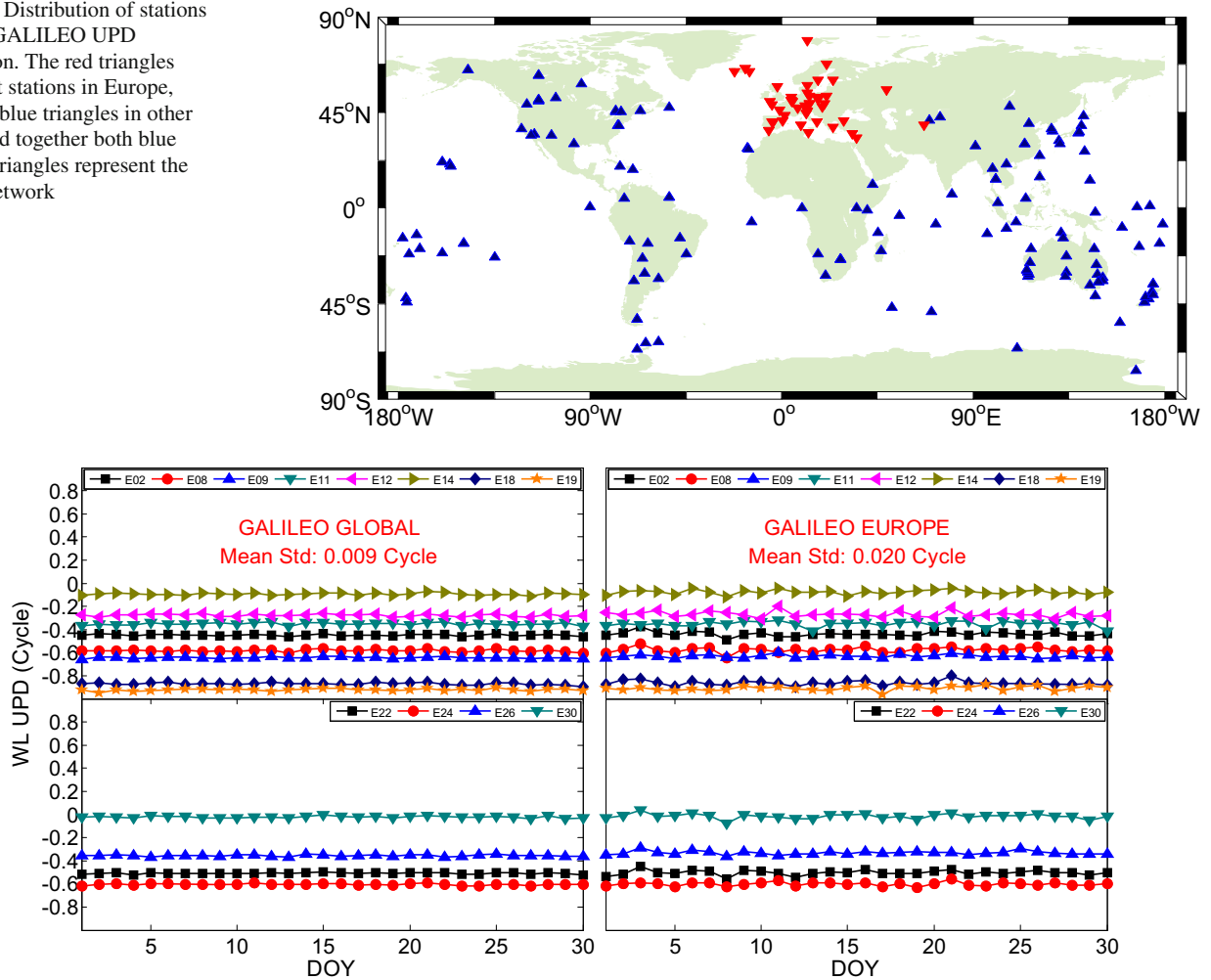
Fig. 20 Estimated Galileo WL UPDs with respect to E01. The left two sub-panels represent the result estimated by global-distributed network, while the right two sub-panels represent the result by European network

Fig. 21 NL UPDs time series of some exemplary Galileo satellites, DOY 001 of 2017
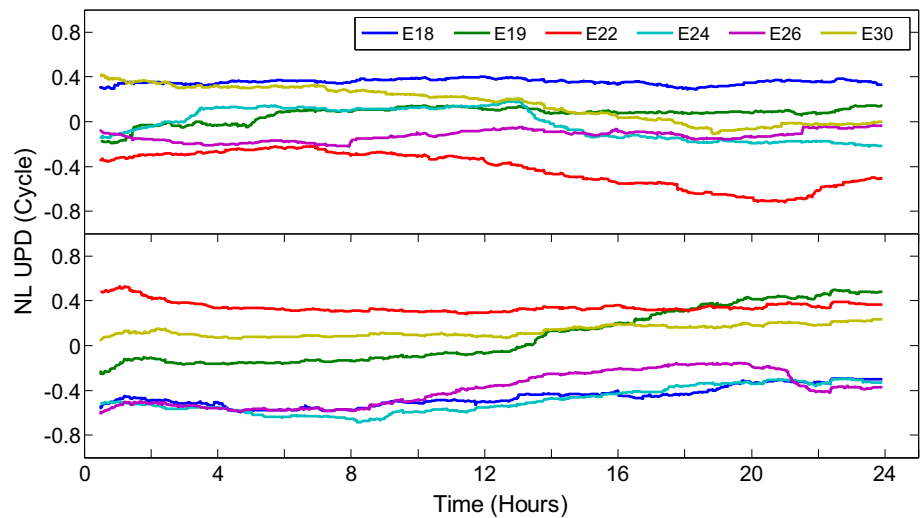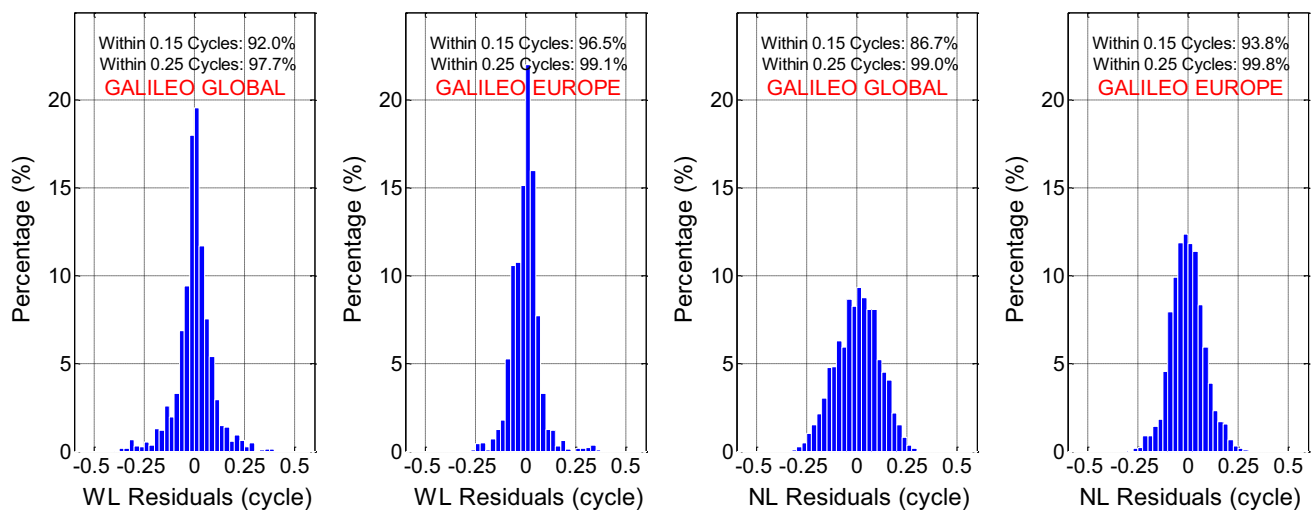
Fig. 22 Distribution of the Galileo WL and NL fractional parts after removal of UPDs. From left to right the four subplots represent WL residuals for global network, WL residuals for European network, NL residuals for global network and NL residuals for European network, respectively

PPP AR performance under different cutoff elevation angles and different session lengths were also assessed.

Figure 23 shows static PPP AR solutions of single-system (G), dual-system (GR, GC and GE), and four-system (GCRE) modes at station KARR, on DOY 001, 2017, which is covered by the BDS service of the Asia-Pacific area. The float and fixed PPP results are shown by the blue and red lines, respectively. It can be clearly seen that the PPP AR solutions shorten the convergence time and improve the position series compared to the float results. The multi-GNSS combination significantly improves the PPP performance of the GPS-only solutions for both float and fixed solutions. And the GCRE PPP AR solutions show best performance in terms of convergence time.

To comprehensively analyze the PPP AR performance, the estimator is restarted every hour to test the convergence time. Figure 24 presents the float and fixed position errors for GCRE PPP solutions from 00:00-23:00 at the BOR1 station on DOY 001 of 2017. The corresponding results from 6:00-11:00 are shown in the Fig. 25. As shown in the figures, with ambiguity fixed, the convergence time and positioning accuracy of GCRE PPP solutions can all be improved. For example, the convergence time of all the sessions is less than 30 min for fixed solutions while some sessions of float results cannot converge to 5 cm in 30 min. Figure 25 shows that some GCRE fixed solutions can converge to 5 cm in a very short time while the float results need more time.

Figure 26 presents the position errors of static PPP AR results for GPS-only, GR and GCRE at BOR1 station from 17:00 to 23:00 on DOY 001 of 2017. As shown in Fig. 26, TTFF is more than 30 min for some GPS-only PPP AR solutions. There is one session of GPS-only results that ambiguity resolution is not achieved. When adding GLONASS,

the TTFF improves to within 15 min for all sessions. Moreover, the combined GCRE PPP AR results present the fastest convergence and the highest accuracy for all three coordinate components.

We also analyzed the static PPP AR performance in single-, dual- and four-system modes under different cutoff ranging from 7° to 30°. The position series of station AUCK are shown in the Fig. 27 as a typical example. We can find that when the cutoff elevation angle is greater than 15°, the accuracy of GPS-only PPP AR results decreases obviously as the cutoff elevation angle increases. When the cutoff angle reaches 30°, the GPS-only PPP AR results are very unreliable while a few centimeters are still achievable in a very short time for GCRE PPP AR solutions.

The convergence time of PPP float solutions and TTFF of PPP AR results under different cutoff elevation angles (from 7° to 30°) are recorded for each station. The statistical results of 22 stations are given in Tables 9 and 10 in Appendix and graphically displayed in Fig. 28. As can be seen in Fig. 28, the PPP float solutions of GPS-only, GE and GC achieved the fastest convergence time with 10° cutoff elevation angle while the solutions of GR and GCRE achieved the fastest convergence time with 20° cutoff elevation angle. When the cutoff elevation angle is increased to 30°, the convergence time for GPS-only and GE PPP solutions increase to 50.68 and 47.18 min while that for GR, GC and GCRE is still less than 30 min. The TTFF of PPP AR results is usually much shorter than the convergence time of PPP float solutions. Compared to the single- and dual-system solutions, the GCRE PPP AR solutions show the shortest TTFF. Taking 7° cutoff elevation angle as example, the average TTFF of static PPP AR solution for GCRE is 9.21 min, which is much shorter than that for GPS (18.07 min), GR (12.10 min), GE

Fig. 23 Static PPP AR solutions of single-system (G),dual-system (GR, GC and GE), and four-system (GCRE) at station KARR, on DOY 001,2017
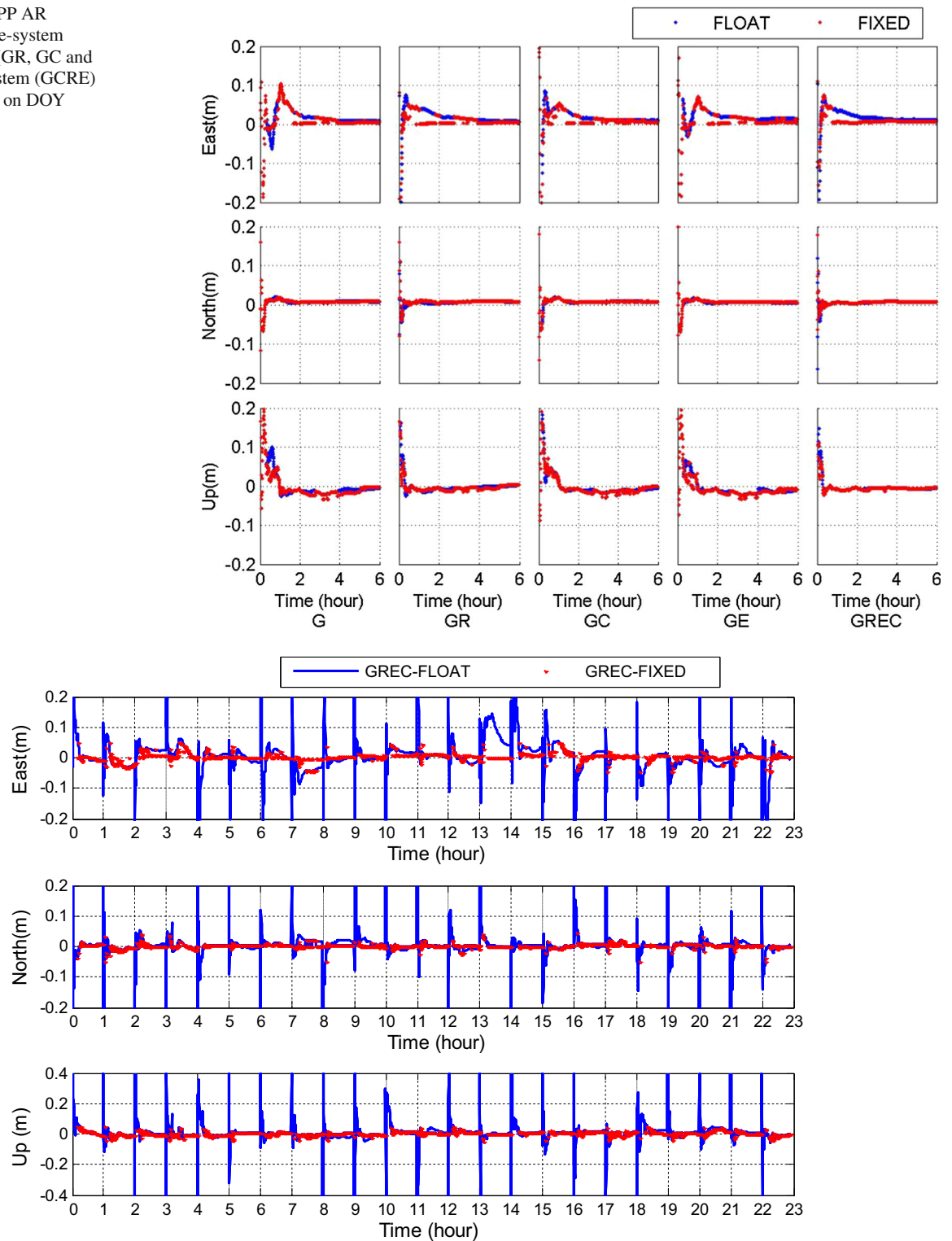

Fig. 24 The float and fixed static PPP results of GCRE for the BOR1 station from 0:00 to 23:00 on DOY 001 of 2017

(15.36 min) and GC (13.21 min). When the cutoff elevation angle is increased to 30° from 7°, the TTFF of GPS and GE PPP AR solutions is increased to 39.95 and 37.36 min from 18.07 and 15.36 min while the results of GR, GC and GCRE is still very stable. It is demonstrated that the accuracy of few centimeters can still be achieved by multi-GNSS PPP AR in a short time (< 10 min) under high cutoff elevation angles while the GPS-only PPP AR require the time about 40 min.

Fig. 25 The float and fixed
static PPP results of GCRE for
the BOR1 station from 6:00 to
11:00 on DOY 1 of 2017
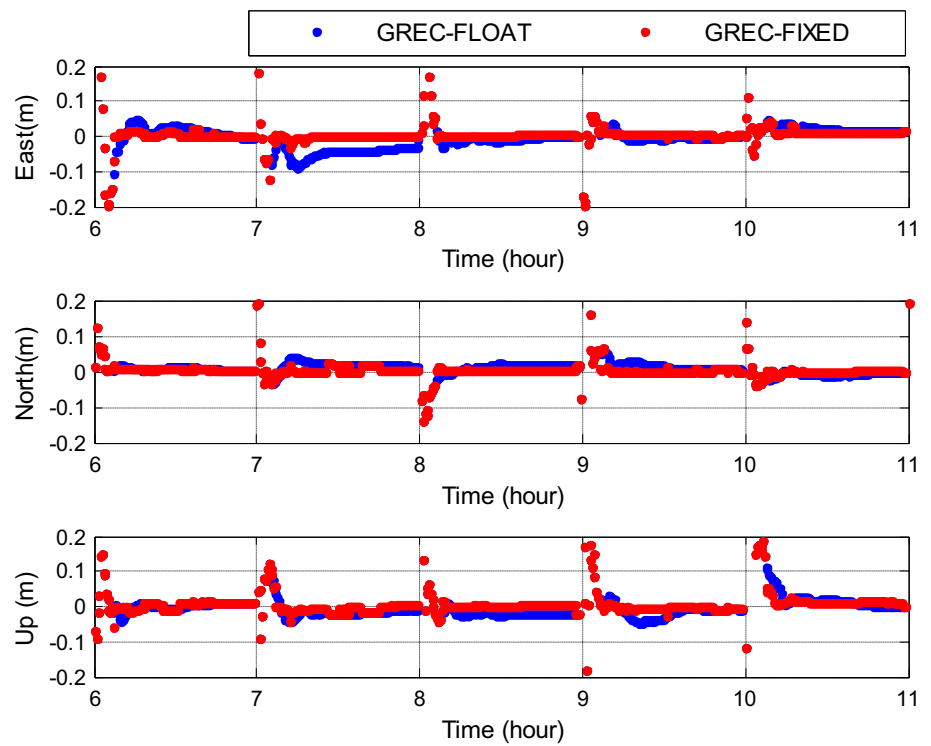
Fig. 26 The static PPP AR
results of GPS-only, GR and
GCRE at BOR1 station from
17:00 to 23:00 on DOY 001 of
2017
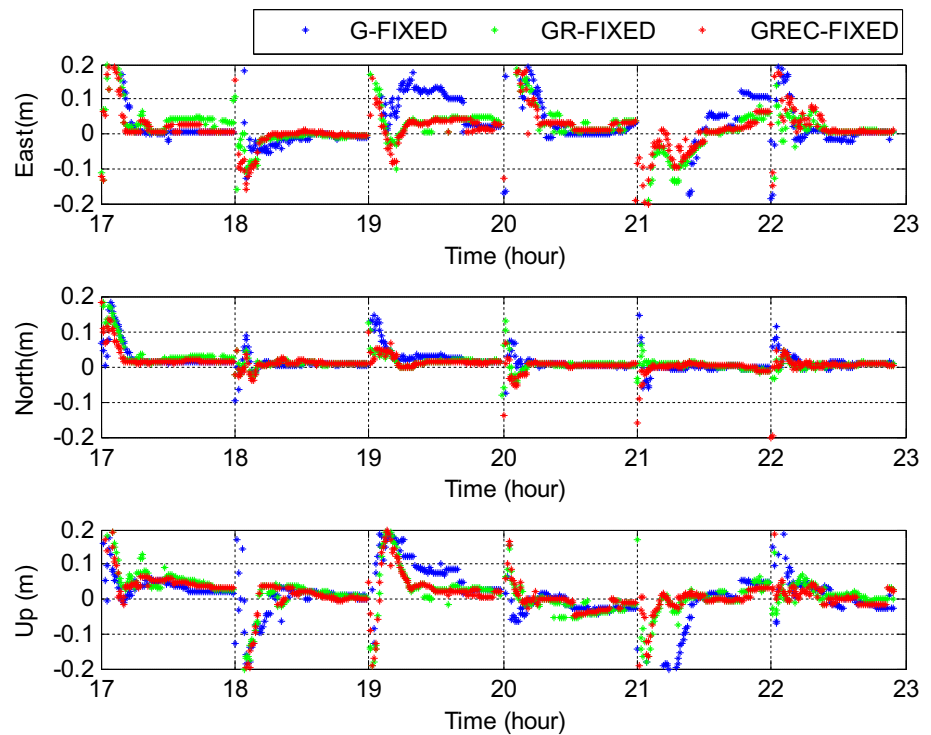
In order to assess the position accuracy of the single-, dual- and four-system PPP ambiguity resolution, float PPP and PPP AR using 10, 20, 30, 60 and 120 min of data from 22 stations on DOY 001, 2017 were carried out. Taking the

session length of 60 min as an example, there were 24 1-hourly solutions for each station if there was no data loss.

Figure 29 shows the statistical results of the PPP float and fixed solutions with different session length, of 10, 20, 30,
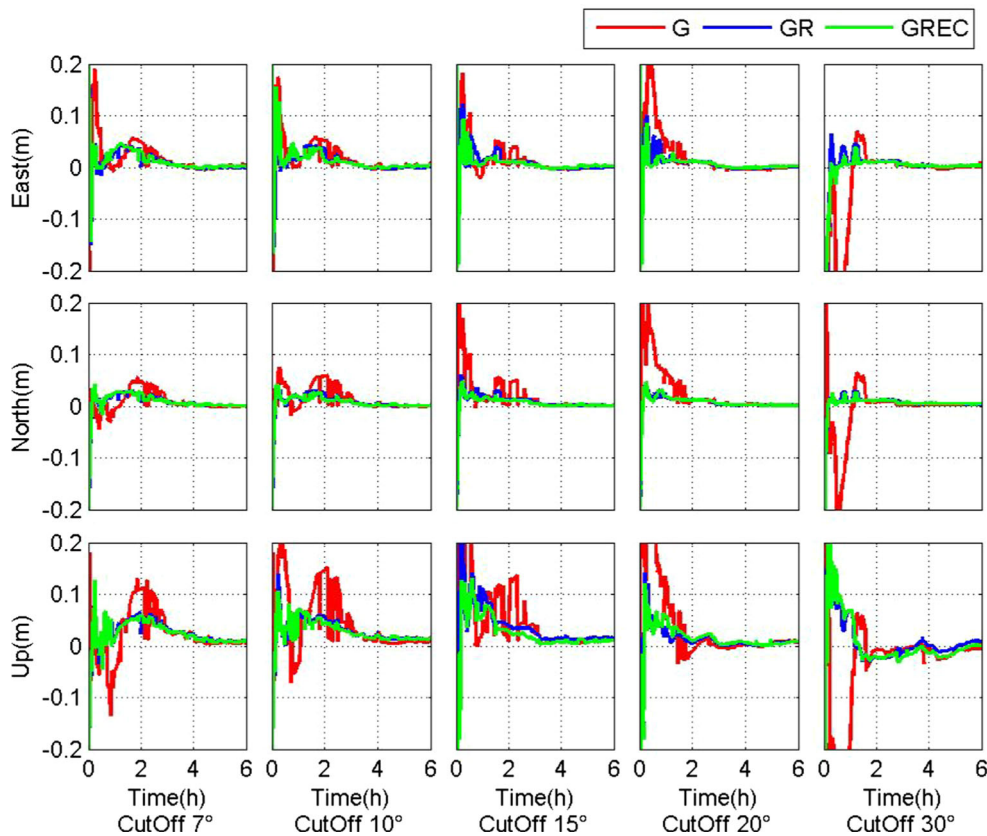
Fig. 27 Static PPP AR results in single-, dual and multi-system modes under different cutoff elevation angles(from 7° to 30°)at station AUCK (GPS Time). The GPS-only, dual-, and four-system solutions are shown by the blue, green and red lines, respectively
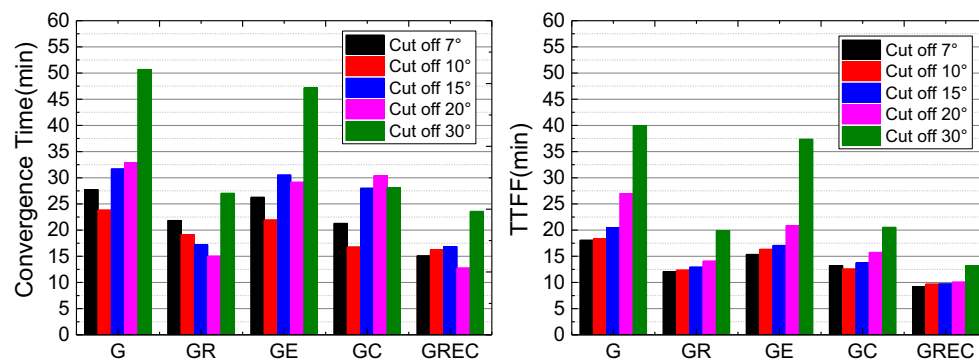

Fig. 28 The average convergence time of static PPP float results and average TTFF of static PPP AR results under different cutoff elevation angles (from 7° to 30°)

60 and 120 min. The float solutions are shown in the left panel while the PPP AR results are shown in the right panel. The root mean square (RMS) values are calculated from all static PPP float solutions over different time sessions while the RMS of PPP AR are calculated from all fixed solutions. The RMS values of float and fixed PPP solutions with different session lengths in single-, dual- and four-system modes are also listed in Tables 11 and 12 in Appendix. As shown in Fig. 29, it can be seen that the positioning accuracy is evi-

dently improved along with the increase of the observational length. The north component is the most accurate component of three components for each system with different session length. With the same session length, the PPP AR results achieve obviously higher accuracy than float solutions. At the 2h-observation session, the accuracy of GCRE PPP AR solutions is (0.44, 0.61, 1.68) cm while the accuracy of float solutions is (1.45, 0.72, 1.88) cm on the east, north vertical direction. Compared to the single- and dual-system results,
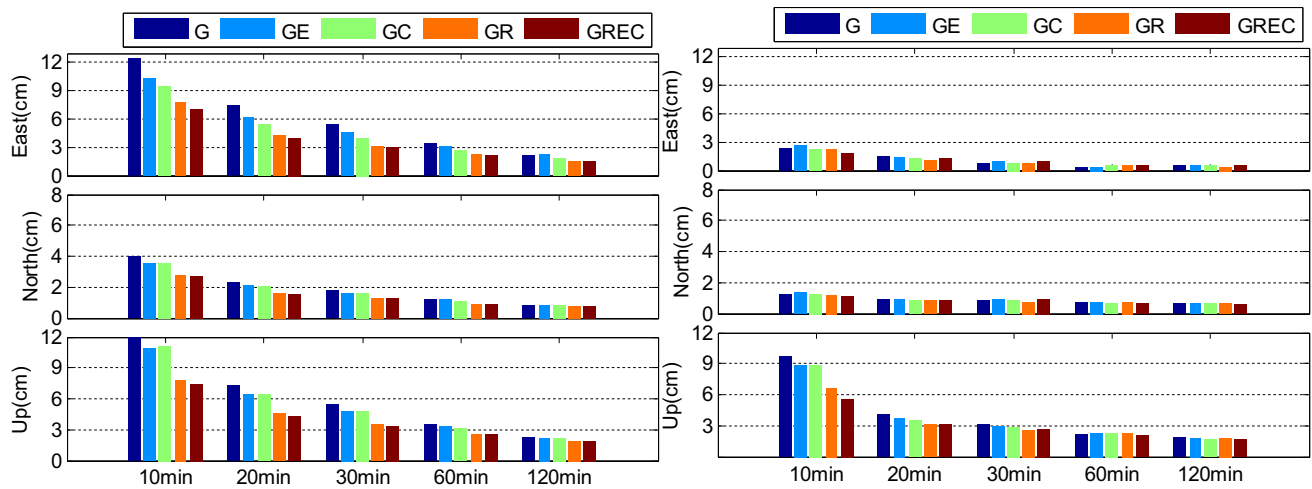
Fig. 29 RMS values of static PPP float and fixed solutions with different session lengths (10, 20, 30, 60 and 120 min) in single-, dual- and four-system modes (left: float; right: fixed)
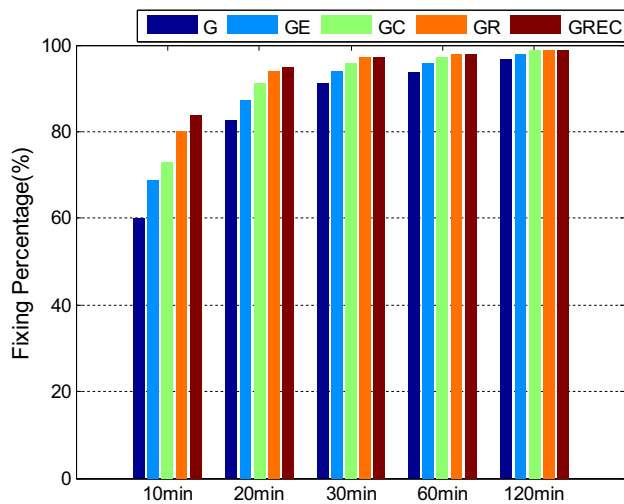
Fig. 30 Fixing percentage of static PPP AR solutions with different session lengths (10, 20, 30, 60 and 120 min) in single-, dual- and four-system modes

GCRE PPP AR can achieve the best accuracy with observations of 10 min. The positioning accuracy of GCRE fixed solution within 10 min is (1.84, 1.11, 1.53) cm while the GPS-only result is (2.25, 1.29, 9.73) cm for the east, north and vertical components.

When the observation session length is increased, the PPP AR results of different systems show the similar positioning accuracy because high percentages of ambiguities are fixed correctly for single-, dual and four-system PPP solutions. Therefore, the ambiguity fixing percentage is an important indicator to assess the performance of PPP AR. The percentage is defined as the percentage of fixed sessions over the total number of sessions. Figure 30 shows the fixing percentage of PPP AR solutions with different session lengths (10, 20, 30, 60 and 120 min). It can be seen that four-system

PPP AR shows the highest fixing percentage with the same session length while the GPS-only PPP AR has the lowest percentage. With the session length less than 20 min, the fixing percentage of GCRE PPP AR is significantly better than single- and dual-system solutions. Taking the result of 10 min as an example, the fixing percentage for GPS-only PPP AR result is only 60.21% and that of dual-system results is 68.88, 72.91 and 80.01% for GE, GC and GR, respectively. Significant improvement is achieved for GCRE result, with the fixing percentage improved to 84.01%. The fixing percentage of PPP AR for single-, dual- and four-system is also summarized in Table 13 in Appendix.

7 Conclusions

This paper presented recent progress made for multi-GNSS PPP ambiguity resolution using GPS+BDS+GLONASS+ Galileo observations. A GCRE four-system UPD estimation model and multi-GNSS undifferenced PPP AR method were developed. With data acquired from MGEX, IGS, CMONOC and HongKong CORS stations, the UPDs of GCRE four systems were estimated, the quality of UPD products in terms of temporal stability and residual distributions were investigated, and were evaluated benefits of multi-GNSS to PPP AR.

A dataset of 30 days from DOY 001 to 030 of 2017 with a tracking network consisting of about 148 MGEX/IGS stations was used for GPS UPD estimation. The mean STD of the 30-day WL UPDs is 0.023 cycles while the mean STD of NL UPDs is 0.04 cycles. The percentage of residuals within ± 0.15 cycles and ± 0.25 cycles are 94.8 and 98.7% for WL, 95.1 and 99.9% for NL, respectively. A global tracking network containing 67 MGEX stations was used to estimate BDS UPDs. The impact study of satellites-induced

biases for BDS resulted in a significant improvement of WL UPDs, particularly for IGSO and MEO satellites (> 75%). Minor improvement was observed for NL UPDs (< 25%). Besides, the WL UPDs estimated from the CMONOC and Hong Kong CORS network were also improved after the code bias correction, especially for MEO satellites (> 70%). No obvious improvement was found for NL UPDs of regional network. When compared with global BDS NL UPDs, BDS NL UPDs estimated by Hong Kong CORS network is more stable with mean STDs of 0.029, 0.013, and 0.007 cycles for GEO, IGSO, and MEO satellites. Thus, it is demonstrated that the higher temporal stability will be achieved for WL UPDs after the code bias correction and the small network will lead to a better result of NL UPDs. With a network of homogeneous receivers, the GLONASS UPDs were estimated with three commonly used receivers (TRIMBLE NETR9, JAVAD TRE_G3TH DELTA and LEICA), respectively. The stable WL UPDs with the mean STD less than 0.06 cycles and NL UPDs with the mean STD less than 0.11 cycles can be estimated with all three types of receivers. Results demonstrate that the UPD values of inhomogeneous receivers are different each other, however, different firmware versions seem to have no effect of the UPDs for the same type of receiver for TRIMBLE NETR9 or LEICA receivers. Global and European networks were applied for the estimation of Galileo UPDs. Both two networks can estimate stable WL UPDs with the mean STD less than 0.02 cycles and NL UPDs with the mean STD less than 0.11 cycles. The mean STD of global-network-derived UPDs were comparable to those from European network. However, the RMS of WL and NL residuals are 0.091 and 0.107 cycles for global network, 0.072 and 0.082 cycles for European network, which indicates that UPDs estimated by European network are more reliable.

The GREC UPD results were then applied to multi-GNSS PPP AR and the performance of the GCRE-combined PPP AR was also investigated and compared with single-system (G) and dual-system (GR, GC, GE). Data collected at 22 MGEX stations were used to analyze the performance of multi-GNSS PPP AR. Compared to the traditional float solutions, PPP AR can shorten the convergence time and improve the positioning accuracy. The combined GCRE PPP AR results present the fastest convergence and the highest accuracy for all three coordinate components compared to single- and dual-system PPP AR solutions. The convergence time of PPP float solutions and TTFF of PPP AR results under different cutoff elevation angles (from 7° to 30°)are recorded for each station. When the cutoff elevation angle is increased to 30°, the convergence time for GPS-only and GE PPP float solutions increase to 50.68 and 47.18 min while that for GR, GC and GCRE is still less than 30 min. Average TTFF of static PPP AR solution with 7° cutoff elevation angle for GCRE is 9.21 min, which is much shorter than that for GPS (18.07 min), GR (12.10 min), GE (15.36 min) and GC (13.21 min). When the cutoff elevation angle is increased to 30° from 7°, the TTFF of GPS and GE PPP AR solutions is increased significantly (> 35 min) while the results of GCRE is still very stable with the TTFF of 13.24 min.

With the same session length, the PPP AR results achieve obviously higher accuracy than float solutions. At the 2h-observation session, GCRE PPP AR solutions improve the positioning accuracy of the float solutions with the improvements of 69.6, 15.2 and 10.6% for the east, north and vertical direction. Compared to the single- and dual-system results, GCRE PPP AR can achieve the best accuracy with observations of 10 min. The positioning accuracy of GCRE fixed solution within 10 min is (1.84, 1.11, 1.53) cm while the GPS-only result is (2.25, 1.29, 9.73) cm for the east, north and vertical components. The GCRE PPP AR shows highest fixing percentage with the same session length while the GPS-only PPP AR has the lowest percentage. when the session length is 10 min, the fixing percentage of GCRE PPP AR solution is 84.01% while the fixing percentage of GPS-only, GE, GC and GR PPP AR solutions are 60.21, 68.88, 72.91 and 80.01%, respectively.

Appendix

Table 7 Percentages of residuals within ±0.15 cycles and ±0.25 cycles of WL and NL UPDs before and after the code bias correction

	WL UPD				NL UPD			
	uncorrected		corrected		uncorrected		corrected	
	±0.15 cycles (%)	±0.25 cycles (%)	±0.15 cycles (%)	±0.25 cycles (%)	±0.15 cycles (%)	±0.25 cycles (%)	±0.15 cycles (%)	±0.25 cycles (%)
GEO	66.5	82.9	60.7	81.1	70.2	98.7	71.8	100
IGSO	66.9	85.6	73.2	88.1	95.8	98.6	96.0	100
MEO	52.6	81.2	71.1	87.1	93.3	95.7	94.9	98.9

Table 8 Percentages of residuals within ± 0.15 cycles and ± 0.25 cycles of WL and NL UPDs estimated from different types of receivers

		TRIMBLE NETR9 all version (%)	TRIMBLE NETR9 5.15 (%)	LEICA (%)	JAVAD TRE_G3TH DELTA (%)
WL UPD (cycles)	± 0.15	76.87	79.08	79.02	68.33
	± 0.25	92.90	94.68	93.41	85.89
NL UPD (cycles)	± 0.15	75.97	74.99	75.74	81.06
	± 0.25	98.82	99.00	99.15	99.13

Table 9 The average convergence time (min) of static PPP float solution under different cutoff elevation angles (from 7° to 30°)

System	7°	10°	15°	20°	30°
G	27.74	23.83	31.69	32.88	50.68
GR	21.83	19.13	17.21	15.02	27.02
GE	26.26	21.95	30.52	29.14	47.18
GC	21.29	16.78	28.00	30.38	28.14
GCRE	15.10	16.30	16.83	12.76	23.57

Table 10 The average TTFF (min) of static PPP AR solution under different cutoff elevation angles (from 7° to 30°)

System	7°	10°	15°	20°	30°
G	18.07	18.33	20.50	27.00	39.95
GR	12.10	12.36	12.93	14.07	19.93
GE	15.36	16.33	17.07	20.86	37.36
GC	13.21	12.57	13.76	15.74	20.52
GCRE	9.21	9.69	9.74	10.07	13.24

Table 11 RMS values of static PPP float solutions with different session lengths (10, 20, 30, 60, 120 min) in single-, dual- and four-system modes (Unit: cm)

System	Direction	10 min	20 min	30 min	60 min	120 min
G	E	12.53	7.43	5.41	3.45	2.17
	N	4.01	2.36	1.77	1.22	0.83
	U	12.72	7.37	5.53	3.55	2.29
GE	E	10.35	6.08	4.48	3.09	2.22
	N	3.59	2.16	1.63	1.15	0.83
	U	10.86	6.4	4.81	3.33	2.19
GC	E	9.5	5.39	3.98	2.61	1.76
	N	3.58	2.1	1.59	1.11	0.8
	U	11.2	6.36	4.8	3.14	2.12
GR	E	7.73	4.3	3.16	2.19	1.49
	N	2.78	1.63	1.29	0.94	0.72
	U	7.89	4.53	3.5	2.61	1.95
GCRE	E	6.98	3.96	2.96	2.07	1.45
	N	2.66	1.58	1.26	0.93	0.72
	U	7.39	4.34	3.36	2.52	1.88

Table 12 RMS values of static PPP AR solutions with different session lengths(10, 20, 30, 60, 120 min) in single-,dual- and four-system modes (Unit: cm)

System	Direction	10 min	20 min	30 min	60 min	120 min
G	E	2.35	1.47	0.86	0.43	0.48
	N	1.29	0.96	0.86	0.75	0.62
	U	9.73	4.2	3.14	2.19	1.86
GE	E	2.61	1.38	0.9	0.42	0.45
	N	1.37	0.88	0.89	0.72	0.68
	U	8.94	3.8	2.94	2.31	1.84
GC	E	2.61	1.38	0.9	0.42	0.45
	N	1.25	0.86	0.83	0.7	0.63
	U	8.94	3.53	2.86	2.26	1.71
GR	E	2.25	1.13	0.73	0.44	0.43
	N	1.19	0.79	0.78	0.71	0.63
	U	6.68	3.05	2.58	2.29	1.78
GCRE	E	1.84	1.29	0.9	0.44	0.44
	N	1.11	0.84	0.88	0.67	0.61
	U	5.59	3.1	2.68	2.04	1.68

Table 13 Fixing percentage with different session lengths for single-, dual- and four-system static PPP

Time (min)	G (%)	GE (%)	GC (%)	GR (%)	GCRE (%)
10	60.21	68.88	72.91	80.01	84.01
20	82.54	87.41	91.11	93.97	95.03
30	91.22	93.86	95.87	97.14	97.35
60	93.79	95.86	97.31	97.93	97.72
120	96.54	97.84	98.70	98.70	98.70

References

Bisnath S, Gao Y (2008) Current state of precise point positioning and future prospects and limitations. In: Sideris MG (ed) Observing our changing earth. Springer, New York, pp 615–623

China Satellite Navigation Office (CSNO) (2012) BeiDou navigation satellite system signal in space interface control document. http://gge.unb.ca/test/beidou_icd_english.pdf

Collins P, Lahaye F, Herous P, Bisnath S (2008) Precise point positioning with AR using the decoupled clock model. In: Proceedings of the ION GNSS 2008, Savannah, 16–19 Sept, pp 1315–1322

de Selding PB (2014) ESA proceeding with Galileo launches despite in-orbit satellite issues. SpaceNews. http://spacenews.com/41616esa-proceeding-with-galileo-launches-despite-in-orbitsatellite-Issues

Dong D, Bock Y (1989) Global positioning system network analysis with phase ambiguity resolution applied to crustal deformation studies in California. J Geophys Res 94(B4):3949–3966

Feng Y, Wang J (2008) GPS RTK performance characteristics and analysis. J Glob Position Syst 7(1):1–8

Gabor MJ, Nerem RS (1999) GPS carrier phase AR using satellite single difference. In: Proceedings of the ION GNSS 1999, Institute of Navigation, Nashville, 14–17 Sept, pp 1569–1578

Gao W, Gao C, Pan S, Wang D, Deng J (2015) Improving ambiguity resolution for medium baselines using combined GPS and BDS dual/triple-frequency observations. Sensors 15(11):27525–27542

Ge M, Gendt G, Rothacher M, Shi C, Liu J (2008) Resolution of GPS carrier phase ambiguities in precise point positioning (PPP) with daily observations. J Geod 82(7):389–399

Geng J, Teferle FN, Shi C, Meng X, Dodson AH, Liu J (2009) Ambiguity resolution in precise point positioning with hourly data. GPS Solut 13(4):263–270

Geng J, Teferle FN, Meng X, Dodson AH (2011) Towards PPP-RTK: ambiguity resolution in real-time precise point positioning. Adv Space Res 47(10):1664–1673

Geng J, Bock Y (2016) GLONASS fractional-cycle bias estimation across inhomogeneous receivers for PPP ambiguity resolution. J Geod 90(4):379–396

Han S (1997) Quality-control issues relating to instantaneous ambiguity resolution for real-time GPS kinematic positioning. J Geod 71(6):351–361

Hatch R (1982) The synergism of GPS code and carrier measurements. In: Proceedings of the third international symposium on satellite Doppler positioning at Physical Sciences Laboratory of New Mexico State University, 8–12 Feb, vol 2, pp 1213–1231

Hofmann-Wellenhof B, Lichtenegger H, Wasle E (2008) GNSS: global navigation satellite systems: GPS, Glonass, Galileo, and more. Springer, New York

Kouba J, Héroux P (2001) Precise point positioning using IGS orbit and clock products. GPS Solut 5(2):12–28

Kouba J (2009) A guide to using International GNSS Service (IGS) products. http://igscb.jpl.nasa.gov/igscb/resource/pubs/UsingIGSProductsVer21.pdf

Laurichesse D, Mercier F, Berthias JP, Broca P, Cerri L (2009) Integer ambiguity resolution on undifferenced GPS phase measurements and its application to PPP and satellite precise orbit determination. Navigation 56(2):135–149

Li P, Zhang X (2015) Precise point positioning with partial ambiguity fixing. Sensors 15(6):13627–13643

Li P, Zhang X, Ren X, Zuo X, Pan Y (2016) Generating gps satellite fractional cycle bias for ambiguity-fixed precise point positioning. Gps Solut 20(4):1–12

Li X, Ge M, Zhang H, Wickert J (2013) A method for improving uncalibrated phase delay estimation and ambiguity-fixing in real-time precise point positioning. J Geod 87:405–416

Li X, Zhang X, Ge M (2011) Regional reference network augmented precise point positioning for instantaneous ambiguity resolution. J Geod 85(3):151–158

Li X, Zhang X (2012) Improving the estimation of uncalibrated fractional phase offsets for PPP ambiguity resolution. Navigation 65(3):513–529

Li X, Dick G, Ge M, Helse S, Wickert J, Bender M (2014) Real-time GPS sensing of atmospheric water vapor: precise point positioning with orbit, clock, and phase delay corrections. Geophys Res Lett 41:3615–3621. https://doi.org/10.1002/2013GL058721

Li X, Ge M, Dai X, Ren X, Fritsche M, Wickert J, Schuh H (2015) Accuracy and reliability of multi-GNSS real-time precise positioning: GPS, GLONASS, BeiDou, and Galileo. J Geod 89:607–635

Liu J, Ge M (2003) PANDA software and its preliminary result of positioning and orbit determination. J Nat Sci Wuhan Univ 8(2B):603–609. https://doi.org/10.1007/BF02899825

Liu Y, Ye S, Song W, Lou Y, Chen D (2017a) Integrating GPS and BDS to shorten the initialization time for ambiguity-fixed PPP. GPS Solut 21(2):333–343

Liu Y, Song W, Lou Y, Ye S, Zhang R (2017b) GLONASS phase bias estimation and its PPP ambiguity resolution using homogeneous receivers. GPS Solut 21(2):427–437

Liu Y, Ye S, Song W, Lou Y, Gu S (2017c) Rapid PPP ambiguity resolution using GPS+GLONASS observations. J Geod 91(4):441–455

Loyer S, Perosanz F, Mercier F, Capdeville H, Marty J (2012) Zero-difference GPS ambiguity resolution at CNES-CLS IGS analysis center. J Geod 86(11):991–1003

Melbourne WG (1985) The case for ranging in GPS-based geodetic systems. In: Proceedings of the first international symposium on precise positioning with the global positioning system, Rockville, 15–19 April

Montenbruck O, Steigenberger P, Khachikyan R, Weber G, Langley RB, Mervart L, Hugentobler U (2014) IGSMGEX: preparing the ground for multi-constellation GNSS science. Inside GNSS 9(1):42–49

Montenbruck O, Steigenberger P, Prange L, Deng Z, Zhao Q, Perosanz F, Romero I, Noll C, Stürze A, Weber G, Schmid R, Macleod K, Schaer S (2017) The multi-GNSS experiment (MGEX) of the international GNSS service (IGS)—achievements, prospects and challenges. Adv Space Res 59:1671–1697

Reussner N, Wanninger L (2011) GLONASS inter-frequency biases and their effects on RTK and PPP carrier phase ambiguity resolution. In: Proceedings of the ION GNSS 2011, Institute of Navigation, Portland, 19–23 Sept, pp 712–716

Rizos C, Montenbruck O, Weber R, Neilan R, Hugentobler U (2013) The IGS MGEX experiment as a milestone for a comprehensive multi-GNSS service. In: Proceedings of ION PNT 2013, Institute of Navigation, Honolulu, pp 289–295

Teunissen PJG (1990) An integrity and quality control procedure for use in multi sensor integration. In: Proceedings ION-GPS, pp 513–522

Teunissen PJG (1995) The least-squares ambiguity decorrelation adjustment: a method for fast GPS integer ambiguity estimation. J Geod 70(1–2):65–82

Teunissen PJG, Joosten P, Tiberius CCJM (1999) Geometry-free ambiguity success rates in case of partial fixing[J]. In: Proceedings of the National Technical Meeting of the Institute of Navigation, pp 201–207

Urlichich Y, Subbotin V, Stupak G, et al (2011) GLONASS modernization. In: ION GNSS+ 2011. pp 3125–3128

Uhlemann M, Gendt G, Ramatschi M, Deng Z (2015) GFZ global multi-GNSS network and data processing results. In: International Association of Geodesy Symposia, pp 673–679

Wang G, Jong KD, Zhao Q, Hu Z, Guo J (2015) Multipath analysis of code measurements for BeiDou geostationary satellites. GPS Solut 19(1):129–139

Wanninger L (2012) Carrier phase inter-frequency biases of GLONASS receivers. J Geod 86(2):139–148

Wanninger L, Beer S (2015) BeiDou satellite-induced code pseudorange variations: diagnosis and therapy. GPS Solut 19(4):639–648

Wübbena G (1985) Software developments for geodetic positioning with GPS using TI-4100 code and carrier measurements. In: Proceedings of the first international symposium on precise positioning with the global positioning system, Rockville

Yamada H, Takasu T, Kubo N, Yasuda A (2010) Evaluation and calibration of receiver inter-channel biases for RTK-GPS/GLONASS. In: Proceedings of the ION GNSS 2010, Institute of Navigation, Portland, 21–24 Sept, pp 1580–1587

Zumberge JF, Heflin MB, Jefferson DC, Watkins MM, Webb FH (1997) Precise point positioning for the efficient and robust analysis of GPS data from large networks. J Geophys Res 102(B3):5005–5017